Petroleum Science 22 (2025) 653–669

Contents lists available at ScienceDirect

Petroleum Science

journal homepage: www.keaipublishing.com/en/journals/petroleum-science

Original Paper

A high-efficiency Q-compensated pure-viscoacoustic reverse time migration for tilted transversely isotropic media

Qiang Mao, Jian-Ping Huang *, Xin-Ru Mu, Yu-Jian Zhang

Geosciences Department, China University of Petroleum (East China), Qingdao, 266580, Shandong, China

ARTICLE INFO

Article history:
Received 2 June 2024
Received in revised form
1 August 2024
Accepted 11 October 2024
Available online 12 October 2024

Edited by Meng-Jiao Zhou and Jie Hao

Keywords:
Anisotropy
Attenuation
FD modeling
Reverse-time migration

ABSTRACT

The attenuation and anisotropy characteristics of real earth media give rise to amplitude loss and phase dispersion during seismic wave propagation. To address these effects on seismic imaging, viscoacoustic anisotropic wave equations expressed by the fractional Laplacian have been derived. However, the huge computational expense associated with multiple Fast Fourier transforms for solving these wave equations makes them unsuitable for industrial applications, especially in three dimensions. Therefore, we first derived a cost-effective pure-viscoacoustic wave equation expressed by the memory-variable in tilted transversely isotropic (TTI) media, based on the standard linear solid model. The newly derived wave equation featuring decoupled amplitude dissipation and phase dispersion terms, can be easily solved using the finite-difference method (FDM). Computational efficiency analyses demonstrate that wavefields simulated by our newly derived wave equation are more efficient compared to the previous pure-viscoacoustic TTI wave equations. The decoupling characteristics of the phase dispersion and amplitude dissipation of the proposed wave equation are illustrated in numerical tests. Additionally, we extend the newly derived wave equation to implement Q-compensated reverse time migration (RTM) in attenuating TTI media. Synthetic examples and field data test demonstrate that the proposed Q-compensated TTI RTM effectively migrate the effects of anisotropy and attenuation, providing high-quality imaging results.

1. Introduction

The anelasticity and anisotropy properties of Earth's media are critical for seismic wave propagation, and have been confirmed by the field observation and laboratory experiments (McDonal et al., 1958; Thomsen, 1986; Carcione, 1992; Robertsson et al., 1994; Aki et al., 1980; Best et al., 2007; Usher et al., 2017). The intrinsic attenuation of subsurface media can result in amplitude loss and phase distortion in seismic waves (Carcione et al., 1988; Zhu et al., 2007). On the other hand, the anisotropic properties of underground media influence the velocity of seismic wave propagation in various directions. Furthermore, attenuation and anisotropy often coexist in certain geological structures (e.g., aligned fluid-filled cracks), simultaneously affecting seismic wave propagation characteristics (Da Silva et al., 2019a; Zhu et al., 2019; Mu et al., 2022). Neglecting the influences of attenuation and anisotropy in migration imaging (e.g., reverse time migration (RTM)) will lead to the inaccurate imaging results (Qu et al., 2017), thereby reducing the precision of geological interpretation. As a result, in order to obtain high-quality imaging results, there is a necessity to develop an efficient and reliable imaging technique in attenuating anisotropic media.

Seismic wave propagation in attenuating media is usually accompanied by amplitude dissipation and phase dispersion (Zhu and Harris, 2014; Shen et al., 2018a; Mu et al., 2021). Failure to account for attenuation effects during imaging processing can result in reduced amplitude and distorted events in the imaged profile (Wang et al., 2018). To describe the inherent attenuation characteristics of subsurface media, the standard linear solid (SLS) (Emmerich and Korn, 1987; Liu et al., 1976; Carcione et al., 1988) and constant Q model (Kjartansson, 1979; Carcione et al., 2002; Wang et al., 2020) are two widely used attenuation theories. By superimposing multiple SLS bodies in parallel across the frequency range of seismic exploration (Emmerich and Korn, 1987; Zhu et al., 2013), the approximate constant Q behavior can be described

* Corresponding author.
E-mail address: jphuang@upc.edu.cn (J.-P. Huang).

https://doi.org/10.1016/j.petsci.2024.10.004

through the SLS attenuation model. Therefore, a series of viscoacoustic wave equations expressed by the memory-variable have recently been derived based on the SLS model for forward modeling and migration imaging (Dutta and Schuster, 2014; Fathalian et al., 2020). Because these equations can be solved using the finite-difference method, they are convenient for practical applications. However, the coupled nature of amplitude attenuation and phase dispersion terms in these wave equations renders them unsuitable for implementing Q-compensated RTM (Zhu et al., 2013; Li et al., 2019). Recently, Mu and Huang (2023) derived a memory-variable expressed viscoacoustic wave equation capable of simulating amplitude attenuation and phase dispersion separately. Another widely used attenuation model is the constant Q model, developed by Kjartansson (1979). Building on the constant Q model, Carcione et al. (2002) formulated a viscoacoustic wave equation expressed through the fractional time derivatives in the time-space domain. Thereafter, Zhu and Harris (2014) derived a time-space domain fractional Laplacian viscoacoustic wave equation, which has been widely used for implementing Q-compensated RTM, owing to its capacity to simulate amplitude attenuation and phase dispersion effects separately (Yang and Zhu, 2018; Ye et al., 2024). Additionally, to handle the spatially variable-order fractional Laplacians in Zhu and Harris's (2014) wave equation, which cannot be well solved by the pseudo-spectral method in heterogeneous media, Chen et al. (2016) proposed a new constant fractional-order time-space domain viscoacoustic wave equation. Moreover, to accurately simulate wave propagation in strongly attenuating media, Mu et al. (2021) presented a viscoacoustic wave equation that outperforms Zhu and Harris's (2014) wave equation in terms of simulation accuracy.

Anisotropy is another crucial characteristic of Earth's media (Thomsen, 1986). The assumption of isotropy will result in an inaccurate depiction of the dynamic and kinematic properties of seismic waves, leading to a loss of resolution in seismic imaging results (Fletcher et al., 2009; Duveneck et al., 2011). Although the full elastic anisotropic wave equations can accurately characterize the anisotropic effects on seismic waves, it requires a significant computational cost in separating the P- and SV-wave mode (Cheng and Fomel, 2014). To reduce computational complexity, many acoustic anisotropic wave equations are derived for wavefield simulations and RTM, under the acoustic assumption (Alkhalifah, 2000). These equations can be mainly divided into two categories: the coupled pseudo-acoustic anisotropic wave equations (Alkhalifah, 2000; Zhou et al., 2006; Duveneck et al., 2011) and pure-acoustic anisotropic wave equations (Chu et al., 2011; Zhan et al., 2012; Xu and Zhou, 2014). The coupled pseudo-acoustic anisotropic wave equation accurately simulates the kinematic features of qP-wave (Huang et al., 2024) and can be conveniently solved by the finite-difference method. However, wavefields simulated through these wave equations contain S-wave artifacts and remain stable only for anisotropic parameters ε no smaller than δ. This is because the acoustic approximation cannot guarantee the S-wave to zero at all phase angle (Grechka et al., 2004). In contrast, wavefields simulated by the pure-acoustic wave equations are free of S-wave artifacts and are numerically stable. Nonetheless, solving pure-acoustic wave equations generally requires spectral-based methods (e.g., pseudo-spectral method). In addition, pure-acoustic wave equation has lower simulation accuracy than coupled pseudo-acoustic anisotropic wave equation due to the additional approximations (e.g., Taylor expansion approximation) adopted in its derivation. In summary, these acoustic anisotropic wave equations have their own advantages and disadvantages, which are of great significance for forward modeling and imaging in anisotropic media.

Recently, some studies have demonstrated the coexistence of anisotropy and attenuation in underground media (Best et al., 2007; Zhubayev et al., 2016), resulting in amplitude reduction and phase distortion of seismic waves (Hao and Alkhalifah, 2019), which has garnered significant research attention. Based on the attenuation mathematical model, many viscoelastic anisotropic (Zhu and Bai, 2019) and viscoacoustic anisotropic wave equations (Xu et al., 2015; Zhang et al., 2020; Da Silva et al., 2019a; Mu et al., 2022) have been developed for describing seismic waves propagation in attenuating anisotropic media. In comparison to viscoelastic anisotropic wave equations, viscoacoustic anisotropic wave equations have been widely used in industrial application for the sake of calculation simplicity. Based on constant Q model and in conjunction with Fletcher et al.'s (2009) coupled pseudo-acoustic anisotropic wave equation, Suh et al. (2012) presented a viscoacoustic VTI wave equation and carried out an RTM algorithm. However, wavefields simulated through these wave equations exhibit undesired S-wave artifacts and cannot remains stable in the case of ε less than δ. To address this issue, Mu et al. (2022) developed a pure-viscoacoustic anisotropic wave equation. Recently, in the context of the new acoustic approximation introduced by Xu et al. (2020), Mao et al. (2024a) derived a high-precision pure-viscoacoustic anisotropic wave equation. These pure-viscoacoustic anisotropic wave equations with decoupled amplitude attenuation and phase dispersion terms, facilitating the realization of Q-compensated RTM. However, solving these wave equations requires multiple fast Fourier transforms (FFTs) and is therefore computationally inefficient. Integrating SLS theory with Cauchy momentum equation and generalized Hooke's law, Da Silva et al. (2019a) derived a viscoacoustic anisotropic wave equation and achieved wavefield simulation using the finite-difference method. This viscoacoustic anisotropic wave equation expressed by the memory-variable, while its amplitude loss and phase dispersion terms are coupled. It is not conducive for implementing Q-compensated RTM. In recent years, some viscoacoustic anisotropic wave equations with the decoupled amplitude attenuation and phase dispersion terms have been derived based on the one-SLS-based attenuation model (Xu et al., 2015; Fathalian et al., 2021). Nevertheless, solving the abovementioned viscoacoustic anisotropic wave equations also require computationally expensive FFTs, making it unsuitable for industrial applications. As a result, the development of an efficient pure-viscoacoustic anisotropic wave equation that can be solved by finite-difference method is necessary.

In this study, we incorporate SLS theory into the pure qP-wave dispersion relation and derive a pure-viscoacoustic TTI wave equation expressed by the memory-variable. The newly derived wave equation can be solved using the finite-difference method, showcasing higher computational efficiency compared to the previous pure-viscoacoustic TTI wave equation expressed by the fractional Laplacians. Then, inspiring by the work of Mu and Huang (2023), we achieve the decoupling of amplitude attenuation and phase dispersion terms of the newly derived pure-viscoacoustic TTI wave equation, facilitating the implementation of Q-compensated RTM in TTI media. Additionally, to reduce artificial reflections from model boundaries (Chen et al., 2014), we adopt the sponge absorbing boundary (Cerjan et al., 1985), as it is simple to implement and does not require modifications to the wave equations. Numerical tests show that the wavefields simulated by the proposed wave equation remain stable and are free of S-wave artifacts. Building on the newly derived wave equation, we implement Q-compensated RTM in TTI media. Two synthetic examples and field data test suggest that the proposed approach can simultaneously correct for attenuation and anisotropy effects, yielding the accurate imaging results.

This paper can be structured as follows. First, we derive a

memory-variable expressed pure-viscoacoustic TTI wave equation with the decoupled amplitude loss and phase dispersion terms. Then, we use some numerical tests to illustrate that our wave equation is S-wave artifacts free and numerically stable. Subsequently, the newly proposed wave equation is used as forward engine to implement Q-compensated RTM in TTI media. Finally, we carry out RTM tasks on synthetic examples and field data to demonstrate the efficacy of the proposed approach.

2. Methodology

To efficiently implement Q-compensated reverse time migration (RTM) in tilted transversely isotropic (TTI) media, we derive a pure-viscoacoustic TTI wave equation featuring decoupled amplitude attenuation and phase dispersion operators. Our new wave equation expressed by the memory-variable and can be solved by the finite-difference method. Subsequently, we extend the newly derived wave equation to realize the Q-compensated RTM in TTI media.

2.1. Pure-viscoacoustic wave equation in tilted transversely isotropic media

To describe the intrinsic attenuation of subsurface media, the standard linear solid (SLS) model is one of the widely used attenuation theories (Robertsson et al., 1994; Carcione et al., 1988; Bai and Tsvankin, 2016; Zhu et al., 2013). In accordance with the SLS model, the viscoacoustic wave equation has been developed for characterizing the propagation properties of seismic waves in attenuating media (Guo et al., 2016; Gu et al., 2022). Some numerical experiments indicate that a viscoacoustic wave equation incorporating one single SLS element can satisfy practical application in attenuating media (Blanch et al., 1995; Zhu et al., 2013). Therefore, the viscoacoustic wave equation with a single SLS in the frequency wavenumber domain can be expressed as

$$\omega^2 P = v_{p0}^2 \left\{ \frac{\tau_\varepsilon}{\tau_\sigma} \left(k_x^2 + k_y^2 + k_z^2 \right) P + \tilde{r} \right\}, \tag{1}$$

$$i\omega \tilde{r} = -\frac{1}{\tau_\sigma} \left\{ \tilde{r} + \left(\frac{\tau_\varepsilon}{\tau_\sigma} - 1 \right) \left(k_x^2 + k_y^2 + k_z^2 \right) P \right\}, \tag{2}$$

where P and $\tilde{r}$ are the spatial Fourier transform of p and r, respectively. r is the memory variable, p is the pressure wavefield, k_x, k_y, and k_z are the wavenumber in the x-, y-, and z-directions. $\tau_\sigma = (\sqrt{Q^2+1}-1)/\omega_0 Q$ and $\tau_\varepsilon = (\sqrt{Q^2+1}+1)/\omega_0 Q$ stand for the stress and strain relaxation times, respectively, where Q is the quality factor, and ω_0 is the reference angular frequency.

In addition, anisotropy stands as another crucial factor influencing the propagation characteristics of seismic waves in subsurface media. For the accurate characterization of seismic wave behavior in anisotropic media, the exact dispersion relation of P- and SV-wave has been established (Tsvankin, 1996), written as

$$\omega_p^2 = \frac{v_{p0}^2}{2} \left((1+2\varepsilon)\left(k_x^2 + k_y^2 \right) + k_z^2 + \frac{v_{s0}^2}{v_{p0}^2} \left(k_x^2 + k_y^2 + k_z^2 \right) + E \right), \tag{3}$$

$$\omega_{sv}^2 = \frac{v_{p0}^2}{2} \left((1+2\varepsilon)\left(k_x^2 + k_y^2 \right) + k_z^2 + \frac{v_{s0}^2}{v_{p0}^2} \left(k_x^2 + k_y^2 + k_z^2 \right) - E \right), \tag{4}$$

$$E = \sqrt{\left((1+2\varepsilon)\left(k_x^2 + k_y^2 \right) - k_z^2 - \frac{v_{s0}^2}{v_{p0}^2} \left(k_x^2 + k_y^2 - k_z^2 \right) \right)^2 + 4 \left(1 - \frac{v_{s0}^2}{v_{p0}^2} \right) \left(1 + 2\delta - \frac{v_{s0}^2}{v_{p0}^2} \right) \left(k_x^2 + k_y^2 \right) k_z^2}, \tag{5}$$

where Eqs. (3) and (4) denote the P- and SV-wave dispersion relation (Liang et al., 2023), respectively. v_{p0} and v_{s0} are P- and SV-wave velocity along the symmetry axis, respectively. ε and δ are Thomsen anisotropy parameters (Thomsen, 1986). Because Eq. (3) involves four parameters (i.e., v_{p0}, v_{s0}, ε, δ), attempts have been made by researchers to simplify it into an equation with only three parameters (i.e., v_{p0}, ε, δ) (Alkhalifah, 2000; Xu et al., 2020). To simplify Eq. (3), Xu et al. (2020) proposed a new acoustic approximation that sets SV-wave phase velocity (V_{sv}) to zero at all phase angles (i.e., $\omega_{sv} = 0$), resulting in a pure qP-wave dispersion relation with only three parameters (Liang et al., 2023), expressed as

$$\omega_p^2 = v_{p0}^2 \left\{ (1+2\varepsilon)\left(k_x^2 + k_y^2 \right) + k_z^2 - S_k \left(k_x^2 + k_y^2 + k_z^2 \right) \right\}, \tag{6}$$

with

$$S_k = \frac{2(\varepsilon - \delta)\left(k_x^2 + k_y^2 \right) k_z^2}{(1+2\varepsilon)\left(k_x^2 + k_y^2 \right)^2 + k_z^4 + (2+2\delta)\left(k_x^2 + k_y^2 \right) k_z^2}. \tag{7}$$

Then, in order to incorporate viscosity into the pure qP-wave dispersion relation, we replace the term $(k_x^2 + k_y^2 + k_z^2)$ in Eqs. (1) and (2) with the term $\{(1+2\varepsilon)(k_x^2 + k_y^2) + k_z^2 - S_k(k_x^2 + k_y^2 + k_z^2)\}$ in Eq. (6), yielding a pure-viscoacoustic wave equation in the frequency-wavenumber domain:

$$\omega^2 P = v_{p0}^2 \left\{ \frac{\tau_\varepsilon}{\tau_\sigma} \left((1+2\varepsilon)\left(k_x^2 + k_y^2 \right) + k_z^2 - S_k \left(k_x^2 + k_y^2 + k_z^2 \right) \right) P + \tilde{r} \right\}, \tag{8}$$

$$i\omega \tilde{r} = -\frac{1}{\tau_\sigma} \left\{ \tilde{r} + \left(\frac{\tau_\varepsilon}{\tau_\sigma} - 1 \right) \left((1+2\varepsilon) \times \left(k_x^2 + k_y^2 \right) + k_z^2 - S_k \left(k_x^2 + k_y^2 + k_z^2 \right) \right) P \right\}. \tag{9}$$

Based on Eqs. (8) and (9), we can simulate the propagation characteristics of seismic waves in attenuating anisotropic media. Transforming Eqs. (8) and (9) into time-space domain, leading to the pure-viscoacoustic VTI wave equation:

$$\frac{\partial^2 p}{\partial t^2} = v_{p0}^2 \left\{ \frac{\tau_\varepsilon}{\tau_\sigma} \left((1+2\varepsilon) \left(\frac{\partial^2 p}{\partial x^2} + \frac{\partial^2 p}{\partial y^2} \right) + \frac{\partial^2 p}{\partial z^2} - S \left(\frac{\partial^2 p}{\partial x^2} + \frac{\partial^2 p}{\partial y^2} + \frac{\partial^2 p}{\partial z^2} \right) \right) - r \right\}, \tag{10}$$

$$\frac{\partial r}{\partial t} = -\frac{1}{\tau_\sigma} \left\{ r - \left(\frac{\tau_\varepsilon}{\tau_\sigma} - 1 \right) \left((1+2\varepsilon) \left(\frac{\partial^2 p}{\partial x^2} + \frac{\partial^2 p}{\partial y^2} \right) + \frac{\partial^2 p}{\partial z^2} - S \left(\frac{\partial^2 p}{\partial x^2} + \frac{\partial^2 p}{\partial y^2} + \frac{\partial^2 p}{\partial z^2} \right) \right) \right\}, \tag{11}$$

$$S = \frac{2(\varepsilon-\delta) \left(\frac{\partial^2}{\partial x^2} + \frac{\partial^2}{\partial y^2} \right) \frac{\partial^2}{\partial z^2}}{(1+2\varepsilon) \left(\frac{\partial^2}{\partial x^2} + \frac{\partial^2}{\partial y^2} \right)^2 + \frac{\partial^4}{\partial z^4} + (2+2\delta) \left(\frac{\partial^2}{\partial x^2} + \frac{\partial^2}{\partial y^2} \right) \frac{\partial^2}{\partial z^2}}, \tag{12}$$

where Eq. (12) is the spatial domain representation of Eq. (7). Eqs. (10) and (11) can be easily solved by the finite-difference method, whereas Eq. (12) can only solved by the spectral-based method. To solve Eq. (12) using the finite-difference method, as per work of Xu and Zhou (2014), the equivalent form of Eq. (7) can be expressed as

$$S_k = \frac{2(\varepsilon-\delta) \left(n_x^2 + n_y^2 \right) n_z^2}{(1+2\varepsilon) \left(n_x^2 + n_y^2 \right)^2 + n_z^4 + (2+2\delta) \left(n_x^2 + n_y^2 \right) n_z^2}, \tag{13}$$

where $\mathbf{n} = (n_x, n_y, n_z) = \mathbf{k}/|\mathbf{k}| = (k_x, k_y, k_z)/|\mathbf{k}|$ denotes the propagation direction of seismic waves, where $|\mathbf{k}| = \sqrt{k_x^2 + k_y^2 + k_z^2}$. Based on the asymptotic approximation that $\mathbf{n} \approx \nabla p / |\nabla p|$ (Xu and Zhou, 2014; Mao et al., 2024b), Eq. (13) can be approximately characterized in the space domain (Liang et al., 2023):

$$S_n \approx \frac{2(\varepsilon-\delta) \left[\left(\frac{\partial p}{\partial x} \right)^2 + \left(\frac{\partial p}{\partial y} \right)^2 \right] \left(\frac{\partial p}{\partial z} \right)^2}{(1+2\varepsilon) \left(\left(\frac{\partial p}{\partial x} \right)^2 + \left(\frac{\partial p}{\partial y} \right)^2 \right)^2 + \left(\frac{\partial p}{\partial z} \right)^4 + (2+2\delta) \left[\left(\frac{\partial p}{\partial x} \right)^2 + \left(\frac{\partial p}{\partial y} \right)^2 \right] \left(\frac{\partial p}{\partial z} \right)^2}. \tag{14}$$

As a result, replacing S in Eqs. (10) and (11) with S_n, we can obtain a new time-space domain pure-viscoacoustic VTI wave equation:

$$\frac{\partial^2 p}{\partial t^2} = v_{p0}^2 \left\{ \frac{\tau_\varepsilon}{\tau_\sigma} \left(2\varepsilon \left(\frac{\partial^2 p}{\partial x^2} + \frac{\partial^2 p}{\partial y^2} \right) + \left(\frac{\partial^2 p}{\partial x^2} + \frac{\partial^2 p}{\partial y^2} + \frac{\partial^2 p}{\partial z^2} \right) (1 - S_n) \right) - r \right\}, \tag{15}$$

$$\frac{\partial r}{\partial t} = -\frac{1}{\tau_\sigma} \left\{ r - \left(\frac{\tau_\varepsilon}{\tau_\sigma} - 1 \right) \times \left(2\varepsilon \left(\frac{\partial^2 p}{\partial x^2} + \frac{\partial^2 p}{\partial y^2} \right) + \left(\frac{\partial^2 p}{\partial x^2} + \frac{\partial^2 p}{\partial y^2} + \frac{\partial^2 p}{\partial z^2} \right) (1 - S_n) \right) \right\}. \tag{16}$$

Eqs. (15) and (16) can be effectively solved by the finite-difference method, markedly enhancing the computational efficiency of wavefields simulation. Additionally, the coordinate transformation relationship between VTI and TTI media is expressed as

$$\begin{aligned} \widehat{k}_x &= \cos(\theta)\cos(\varphi) k_x + \cos(\theta)\sin(\varphi) k_y - \sin(\theta) k_z, \\ \widehat{k}_y &= -\sin(\varphi) k_x + \cos(\varphi) k_y, \\ \widehat{k}_z &= \sin(\theta)\cos(\varphi) k_x + \sin(\theta)\sin(\varphi) k_y + \cos(\theta) k_z, \end{aligned} \tag{17}$$

where θ and φ denotes the tilt angle and azimuth angle, respectively. $\widehat{k}_x$, $\widehat{k}_y$, and $\widehat{k}_z$ are the new wavenumbers in the rotated coordinate system. In the context of Eq. (17), the 2D pure-viscoacoustic TTI wave equation can be written as

$$\frac{\partial^2 p}{\partial t^2} = v_{p0}^2 \left\{ \left(2\varepsilon T_{xx} p + (1 - \bar{S}_n) \left(\frac{\partial^2 p}{\partial x^2} + \frac{\partial^2 p}{\partial z^2} \right) \right) \frac{\tau_\varepsilon}{\tau_\sigma} - r \right\}, \tag{18}$$

$$\frac{\partial r}{\partial t} = -\frac{1}{\tau_\sigma} \left\{ r - \left(\frac{\tau_\varepsilon}{\tau_\sigma} - 1 \right) \left(2\varepsilon T_{xx} p + (1 - \bar{S}_n) \left(\frac{\partial^2 p}{\partial x^2} + \frac{\partial^2 p}{\partial z^2} \right) \right) \right\}, \tag{19}$$

where

$$\bar{S}_n \approx \frac{2(\varepsilon-\delta)(T_x p / T_z p)^2}{1 + (1+2\varepsilon)(T_x p / T_z p)^4 + (2+2\delta)(T_x p / T_z p)^2}, \tag{20a}$$

$$T_{xx} = \cos^2(\theta) \frac{\partial^2}{\partial x^2} - \sin(2\theta) \frac{\partial^2}{\partial x \partial z} + \sin^2(\theta) \frac{\partial^2}{\partial z^2}, \tag{20b}$$

$$T_x = \cos(\theta) \frac{\partial}{\partial x} - \sin(\theta) \frac{\partial}{\partial z}, T_z = \sin(\theta) \frac{\partial}{\partial x} + \cos(\theta) \frac{\partial}{\partial z}. \tag{20c}$$

The 3D pure-viscoacoustic TTI wave equation is detailed in Appendix A. It should be noted that Eq. (20) incorporates coupled amplitude loss and phase dispersion operators, posing challenges for the implementation of Q-compensated RTM. Therefore, it is necessary to derive a pure-viscoacoustic TTI wave equation includes the decoupled amplitude loss and phase dispersion operators.

Theoretically, the pure-viscoacoustic TTI wave propagator W_{vis} can generally be expressed as

$$W_{\text{vis}} = W_{\text{ac}} + W_{\text{phase}} + W_{\text{amp}}, \tag{21}$$

where W_{ac} is pure-acoustic TTI wave propagator, W_{phase} is a phase dispersion controlled operator, W_{amp} is an amplitude loss controlled operator. The combination of W_{ac} and W_{phase} forms the phase dispersion-dominated pure-viscoacoustic TTI wave propagator W_{vpd} (i.e., $W_{\text{vpd}} = W_{\text{ac}} + W_{\text{phase}}$), while the combination of W_{ac} and W_{amp} forms the amplitude loss-dominated pure-viscoacoustic TTI wave propagator W_{vamp} (i.e., $W_{\text{vamp}} = W_{\text{ac}} + W_{\text{amp}}$). Additionally, Mu and Huang (2023) pointed out that the viscoacoustic wave equation can be decoupled by the addition and subtraction of these three operators, and derived a decoupled SLS-based viscoacoustic wave equation. According to this approach, when we first derive a phase dispersion-dominated pure-viscoacoustic TTI wave propagator W_{vpd} (i.e., $W_{\text{vpd}} = W_{\text{ac}} + W_{\text{phase}}$), then we subtract the phase dispersion controlled operator W_{phase} from the pure-viscoacoustic TTI wave propagator W_{vis} can indirectly yield the amplitude loss-dominated pure-viscoacoustic TTI wave propagator W_{vamp} :

$$W_{\text{vamp}} = W_{\text{vis}} - W_{\text{phase}}. \tag{22}$$

Therefore, we can derive the phase dispersion-dominated and amplitude loss-dominated pure-viscoacoustic TTI wave propagators, respectively. Using these two derived wave propagators, we

can further derive a pure-viscoacoustic TTI wave equation that includes decoupled amplitude loss and phase dispersion terms. Based on this analysis, and starting with the one-SLS model and drawing on the derivation by Fathalian et al. (2020), we first derive a phase dispersion-dominated pure-viscoacoustic TTI wave equation W_{vpd} (see Appendix B):

$$\frac{\partial^2 p}{\partial t^2} = v_{\mathrm{p0}}^2 \left(2\varepsilon T_{xx} p + (1-\overline{S}_n)\left(\frac{\partial^2 p}{\partial x^2} + \frac{\partial^2 p}{\partial z^2} \right) \right) \left(1 + \frac{2}{A} - 1 \right). \quad (23)$$

In Eq. (23), the term associated with $2/A - 1$ is a phase dispersion controlled operator W_{phase}. Then, according to Eq. (22), subtracting W_{phase} from Eq. (18) can indirectly yield the amplitude loss-dominated pure-viscoacoustic TTI wave equation W_{vamp}:

$$\frac{\partial^2 p}{\partial t^2} = v_{\mathrm{p0}}^2 \left\{ \left(2\varepsilon T_{xx} p + (1-\overline{S}_n)\left(\frac{\partial^2 p}{\partial x^2} + \frac{\partial^2 p}{\partial z^2} \right) \right) \left(\frac{\tau_\varepsilon}{\tau_\sigma} + 1 - \frac{2}{A} \right) - r \right\}. \quad (24)$$

Based on Eqs. (23) and (24), we derive a new pure-viscoacoustic TTI wave equation with decoupled amplitude loss and phase dispersion, written as

$$\frac{1}{v_{\mathrm{p0}}^2}\frac{\partial^2 p}{\partial t^2} = \left(2\varepsilon T_{xx} p + (1-\overline{S}_n)\left(\frac{\partial^2 p}{\partial x^2} + \frac{\partial^2 p}{\partial z^2} \right) \right) \left(1 + \kappa_1 \left(\frac{2}{A} - 1 \right) + \kappa_2 \left[\frac{\tau_\varepsilon}{\tau_\sigma} - \frac{2}{A} \right] \right) - \kappa_2 r, \quad (25)$$

where $\kappa_1 = 0$ and $\kappa_2 = 0$, Eq. (25) becomes acoustic anisotropic wave equation derived in Liang et al. (2023); $\kappa_1 = 1$ and $\kappa_2 = 0$, Eq. (25) becomes phase dispersion-dominated pure-viscoacoustic TTI wave equation (Eq. (23)); $\kappa_1 = 0$ and $\kappa_2 = 1$, Eq. (25) becomes amplitude loss-dominated pure-viscoacoustic TTI wave equation (Eq. (24)); $\kappa_1 = 1$ and $\kappa_2 = 1$, Eq. (25) is a pure-viscoacoustic TTI wave equation.

2.2. Analysis of decoupled amplitude loss and phase dispersion feature

To demonstrate the behavior of decoupled amplitude loss and phase dispersion of the newly derived pure-viscoacoustic TTI wave equation, we design a homogeneous model for forward modeling. The model is discretized into a grid of 401 × 401 with a mesh interval of 10 m. We adopt a peak frequency of 20 Hz Ricker wavelet as the source, which is injected in (2 km, 2 km). The reference frequency is same as the dominant frequency of source wavelet.

Fig. 1 shows the wavefields snapshots in the homogeneous model. In Fig. 1, it is clearly that the proposed wave equation can simulate the amplitude loss and phase dispersion effects separately. Additionally, Fig. 2(a) depicts the waveforms simulated by the different wave equations, and the corresponding frequency spectrum are plotted in Fig. 2(b). Fig. 2 illustrates that the amplitude-loss dominated wavefield and phase-dispersion dominated wavefield exhibit attenuated amplitude and phase delay, respectively, in comparison to the acoustic case. The waveforms of viscoacoustic wavefield display attenuated amplitude and shifted phase simultaneously. This observation suggests that the newly derived pure-viscoacoustic TTI wave equation is capable of simulating the amplitude dissipation and phase dispersion characteristic separately. This feature facilitates the implementation of Q-compensated RTM in TTI media.

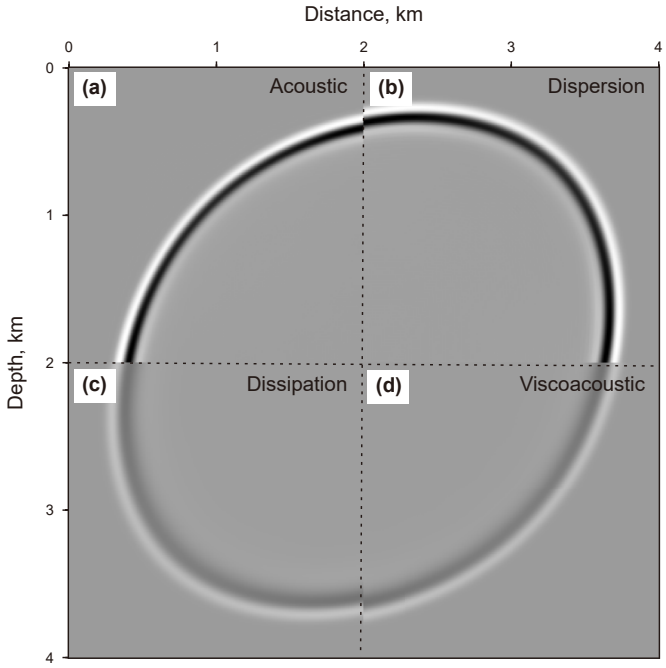

Fig. 1. Wavefield snapshots at 0.6 s simulated by **(a)** acoustic TTI, **(b)** phase dispersion dominated TTI, **(c)** amplitude dissipation dominated TTI and **(d)** viscoacoustic TTI wave equations. The model parameters are $v_{\mathrm{p0}} = 3000$ m/s, $\varepsilon = 0.25$, $\delta = 0.1$, $\theta = 45$, $Q = 20$.

2.3. Analysis of numerical stability, S-wave artifacts and simulation accuracy

The wavefields simulated by the coupled-viscoacoustic TTI wave equation exhibit S-wave artifacts and cannot remain stable in the case of $\varepsilon < \delta$ (Mu et al., 2022). In order to illustrate the newly derived pure-viscoacoustic TTI wave equation shares the same characteristics with the pure qP-wave TTI wave equation, we perform wavefield simulation in the homogeneous attenuating TTI model. The models consist of 501 × 501 grids with a spatial interval of 10 m. The source is a Ricker wavelet with a dominant frequency of 25 Hz, excited at the center of the model. Fig. 3 shows the wavefields simulated by the proposed pure-viscoacoustic TTI wave equation and the coupled pseudo-viscoacoustic TTI wave equation (see Appendix C). It is evident from Fig. 3(d)–(f) that the wavefields simulated by the proposed pure-viscoacoustic TTI wave equation are free of shear wave artifacts and remain numerically stable when the anisotropic parameters $\varepsilon < \delta$, in contrast to those computed by the coupled pseudo-viscoacoustic TTI wave equation (Fig. 3(a)–(c)).

Additionally, Fig. 3(g)–(i) depict the comparison between Fig. 3(a)–(c) and Fig. 3(d)–(f), showcasing the good consistency between the results simulated by the proposed wave equation and those by the coupled pseudo-viscoacoustic TTI wave equation. This observation suggests that the proposed wave equation is capable of accurately simulating seismic wave propagation in attenuating anisotropic media.

2.4. Implementation of Q-compensated reverse time migration

The wave equations describing the propagation of seismic waves serve as the foundation for migration imaging. The newly derived wave equation features decoupled amplitude loss and phase dispersion properties, facilitating the implementation of Q-compensated RTM (Zhu, 2016). To achieve attenuation compensation, reversing the sign (i.e., $\kappa_1 = 1$; $\kappa_2 = -1$) of the amplitude loss

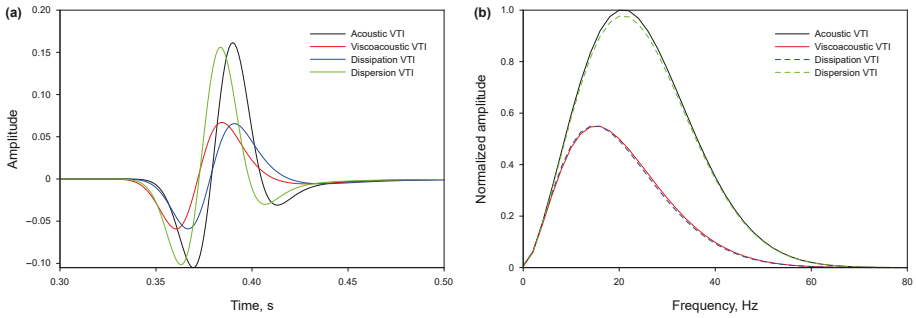

Fig. 2. **(a)** Seismograms comparisons between acoustic TTI, phase dispersion dominated TTI, amplitude dissipation dominated TTI and viscoacoustic TTI wave equations. **(b)** The corresponding amplitude spectrum of Fig. 2(a).

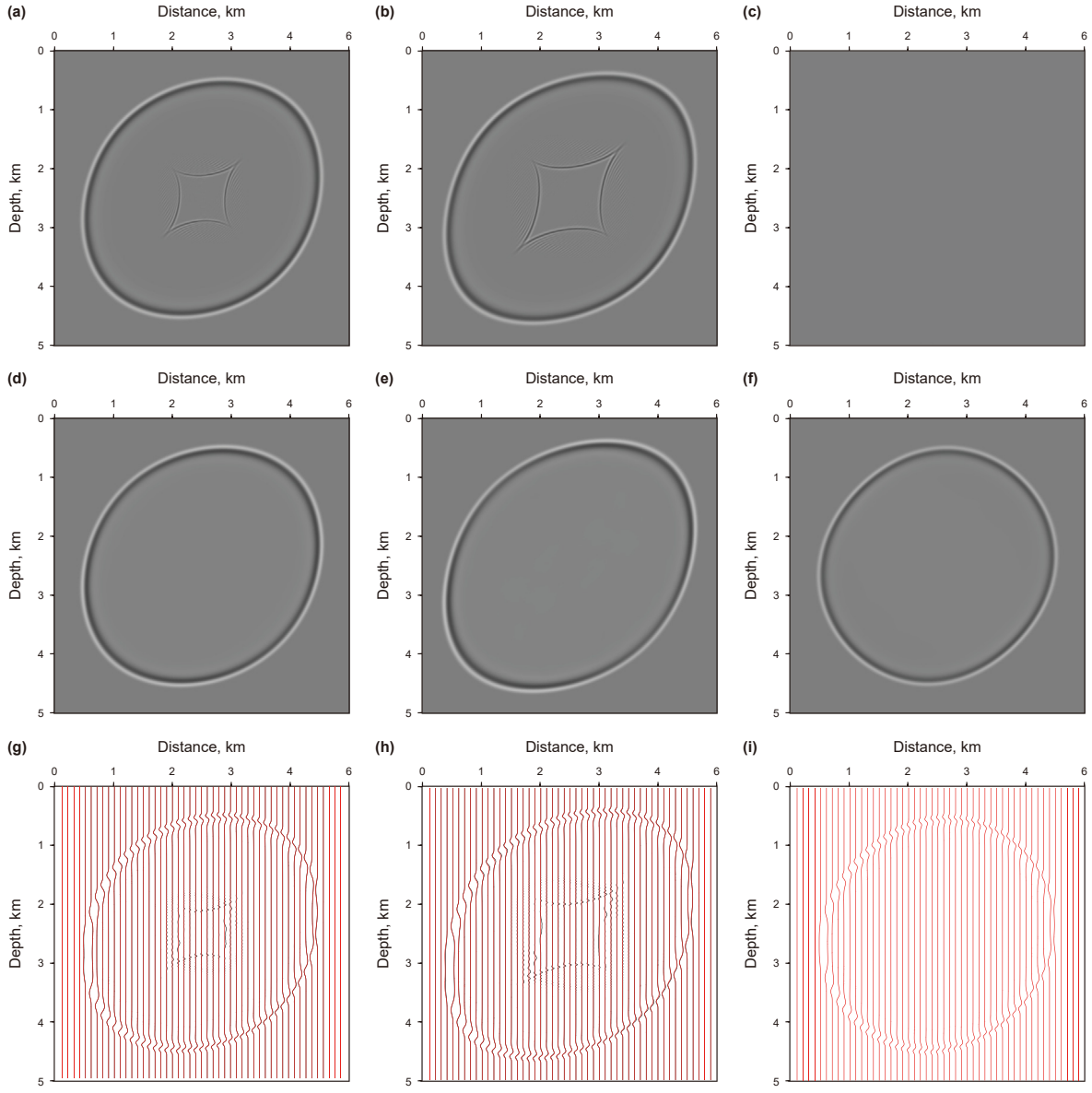

Fig. 3. Wavefield snapshots at 0.7 s in homogeneous model simulated by the different wave equations. **(a–c)** are simulated by the coupled pseudo-viscoacoustic TTI wave equation. **(d–f)** are calculated using the proposed pure-viscoacoustic TTI wave equation. **(g–i)** The superposition of first row (black solid line) and second row (red solid line). The anisotropic parameters in (a) and (d) are $\varepsilon = 0.2$, $\delta = 0.1$, in (b) and (e) are $\varepsilon = 0.35$, $\delta = 0.15$, in (c) and (f) are $\varepsilon = 0.1$, $\delta = 0.2$. The common used parameters are $v_{p0} = 3000$ m/s, $\theta = 45$, $Q = 30$. All snapshots are plotted in the same color scale.

term in Eq. (25) yields the attenuation compensated wavefield modeling operator:

$$\frac{\partial^2 p}{\partial t^2}=v_{\mathrm{p0}}^2\left(2\varepsilon T_{xx}p+(1-\bar{S}_n)\left(\frac{\partial^2 p}{\partial x^2}+\frac{\partial^2 p}{\partial z^2}\right)\right)\left(\frac{4}{A}-\frac{\tau_\varepsilon}{\tau_\sigma}\right)+v_{\mathrm{p0}}^2 r, \tag{26}$$

$$\frac{\partial r}{\partial t}=-\frac{1}{\tau_\sigma}\left\{r-\left(\frac{\tau_\varepsilon}{\tau_\sigma}-1\right)\left(2\varepsilon T_{xx}p+(1-\bar{S}_n)\left(\frac{\partial^2 p}{\partial x^2}+\frac{\partial^2 p}{\partial z^2}\right)\right)\right\}. \tag{27}$$

However, directly reversing the sign of the amplitude loss term may lead to unstable wavefields, attributed to the magnification of the high-frequency components (Xie et al., 2015; Sun and Zhu, 2018; Fathalian et al., 2021). To suppress these high-frequency components, some approaches have been developed, such as the low-pass filter method (Zhu, 2016), stabilization factor method (Wang et al., 2018), regularization method (Tian et al., 2015). Based on the regularization approach, the attenuation compensated wavefield modeling operator with a regularization term can be expressed as

$$\begin{aligned}\frac{\partial^2 p}{\partial t^2}=&v_{\mathrm{p0}}^2\left(2\varepsilon T_{xx}p+(1-\bar{S}_n)\left(\frac{\partial^2 p}{\partial x^2}+\frac{\partial^2 p}{\partial z^2}\right)\right)\left(\frac{4}{A}-\frac{\tau_\varepsilon}{\tau_\sigma}\right)+v_{\mathrm{p0}}^2 r\\&+\zeta v_{\mathrm{p0}}\frac{\partial}{\partial t}\left(2\varepsilon T_{xx}p+(1-\bar{S}_n)\left(\frac{\partial^2 p}{\partial x^2}+\frac{\partial^2 p}{\partial z^2}\right)\right),\end{aligned} \tag{28}$$

where ζ is a regularization parameter, which is empirically chosen and is usually a small positive value close to zero. It plays a crucial role in the stabilization of the attenuation compensated wavefield. To select this parameter accurately, we can perform a simple forward modeling test (Mu et al., 2022) following the two step: First, we use Eq. (26) to simulate the reference wavefield using the low-pass filter developed by Zhu (2016). Second, we select a small positive regularization parameter ζ to simulate wavefield using Eq. (28). The simulated wavefield is compared with the reference result, and then ζ in Eq. (28) is adjusted until the simulated wavefield closely match the reference result, determining the most appropriate regularization parameter. In addition, the imaging condition is another important component in the Q-compensated RTM workflow. This paper employs the source-normalized correlation (SNC) imaging condition proposed by Fathalian et al. (2020) as imaging condition. This is because SNC imaging condition has two advantages: First, the images calculated using the SNC imaging condition in viscoacoustic anisotropic media are theoretically equivalent to those calculated in acoustic anisotropic non-attenuating case. Second, for Q-compensated imaging, the SNC imaging condition only needs to compensate the backward receiver wavefield, unlike the zero-lag correlation imaging condition, which requires compensating both the forward source and the backward receiver wavefield. Therefore, the SNC imaging condition is more convenient and suitable for Q-compensated RTM, written as

$$\begin{aligned}I_C=&\frac{\int_t S_A(\mathbf{x},t)R_C(\mathbf{x},t)\mathrm{d}t}{\int_t S_A(\mathbf{x},t)S_A(\mathbf{x},t)\mathrm{d}t}=\frac{\int_t S_A(\mathbf{x},t)R_A(\mathbf{x},t)\mathrm{e}^{+\alpha L_{\mathrm{up}}}\mathrm{d}t}{\int_t S_A(\mathbf{x},t)S_A(\mathbf{x},t)\mathrm{d}t}\\=&\frac{\int_t S(\mathbf{x},t)\mathrm{e}^{-\alpha L_{\mathrm{down}}}R(\mathbf{x},t)\mathrm{e}^{-\alpha L_{\mathrm{down}}}\mathrm{e}^{-\alpha L_{\mathrm{up}}}\mathrm{e}^{+\alpha L_{\mathrm{up}}}\mathrm{d}t}{\int_t S(\mathbf{x},t)\mathrm{e}^{-\alpha L_{\mathrm{down}}}S(\mathbf{x},t)\mathrm{e}^{-\alpha L_{\mathrm{down}}}\mathrm{d}t},\end{aligned} \tag{29}$$

where α and L denote attenuation coefficient and the propagation length, respectively. The subscripts up and down stand for the upgoing and downgoing waves, respectively. $S(\mathbf{x},t)$ and $R(\mathbf{x},t)$ are source and receiver wavefields in non-attenuating anisotropic media, respectively. $S_A(\mathbf{x},t)=S(\mathbf{x},t)\mathrm{e}^{-\alpha L_{\mathrm{down}}}$, $R_A(\mathbf{x},t)=R(\mathbf{x},t)\mathrm{e}^{-\alpha L_{\mathrm{down}}}\mathrm{e}^{-\alpha L_{\mathrm{up}}}$ are attenuated source wavefields and attenuated receiver wavefields in attenuating anisotropic media, respectively. $R_C(\mathbf{x},t)=R_A(\mathbf{x},t)\mathrm{e}^{+\alpha L_{\mathrm{up}}}=R(\mathbf{x},t)\mathrm{e}^{-\alpha L_{\mathrm{down}}}\mathrm{e}^{-\alpha L_{\mathrm{up}}}\mathrm{e}^{+\alpha L_{\mathrm{up}}}$ is compensated receiver wavefields in attenuating anisotropic media. After simple mathematical operations, Eq. (29) can be rewritten as

$$I_C=\frac{\int_t S(\mathbf{x},t)R(\mathbf{x},t)\mathrm{d}t}{\int_t S(\mathbf{x},t)S(\mathbf{x},t)\mathrm{d}t}=I, \tag{30}$$

where I is an imaging condition in non-attenuating anisotropic media. From Eq. (30), we can conclude that employing the SNC imaging condition in Q-compensated TTI RTM only compensate the receiver wavefield is sufficient to obtain the compensated RTM images. Additionally, the migration results obtained using imaging condition stated in Eq. (29) are consistent with those obtained in non-attenuating media.

3. Numerical examples

In this section, we test the feasibility and efficacy of the proposed Q-compensated TTI RTM using two synthetic examples and one field data set. For the synthetic examples, the observed data are computed using the proposed pure-viscoacoustic TTI wave equation. Additionally, absorbing boundary conditions are necessary in numerical simulations, and the sponge absorbing boundary (Cerjan et al., 1985) with forty damping layers is used to reduce artificial reflections from model boundaries. In all numerical examples, the reference frequency is equal to the dominant frequency of the source wavelet, and the efficient finite-difference method is adopted to solve the newly derived pure-viscoacoustic TTI wave equation.

3.1. BP gas chimney TTI model

First, we perform RTM task in a BP gas chimney TTI model to illustrate the feasibility of the proposed approach. In BP gas chimney TTI model (shown in Fig. 4), a strong attenuation gas chimney is designed in center of the model. This model is discretized into a grid of 401 × 201 points with the grid size of 10 m × 10 m. A Ricker wavelet with a peak frequency of 20 Hz is used as source, and the time step is 0.001 s. In total, 80 shots are evenly placed on the surface with a shot interval of 50 m. To record the reflections, each shot use 401 receivers with a receiver interval of 10 m and the record length is 2.4 s.

Fig. 5(a)–(b) plots the shot gathers simulated by the pure acoustic TTI (i.e., $Q\to\infty$) and pure-viscoacoustic TTI wave equations, respectively. In comparison to acoustic TTI data (Fig. 5(a)), viscoacoustic TTI data exhibit obvious attenuated amplitude (Fig. 5(b)). Additionally, Fig. 5(c) depicts the comparison of single traces between Fig. 5(a) and (b). From Fig. 5(c), revealing significantly phase delay and reduced amplitude in viscoacoustic TTI data compared to acoustic TTI data. This result illustrates that the proposed pure-viscoacoustic TTI wave equation works well in simulating the propagation behavior of seismic waves in attenuating TTI media.

In addition, Fig. 6(a)–(b) show the wavefields simulated by the proposed wave equation and coupled pseudo-viscoacoustic TTI

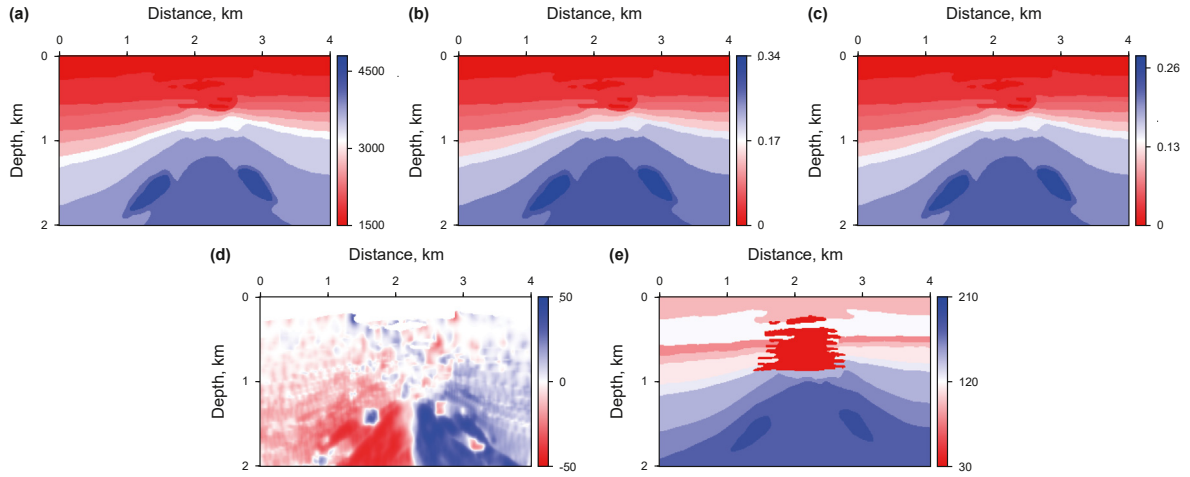

Fig. 4. The model parameters of BP gas chimney TTI model: **(a)** velocity model, **(b)** ε model, **(c)** δ model, **(d)** θ model, and **(e)** Q model.

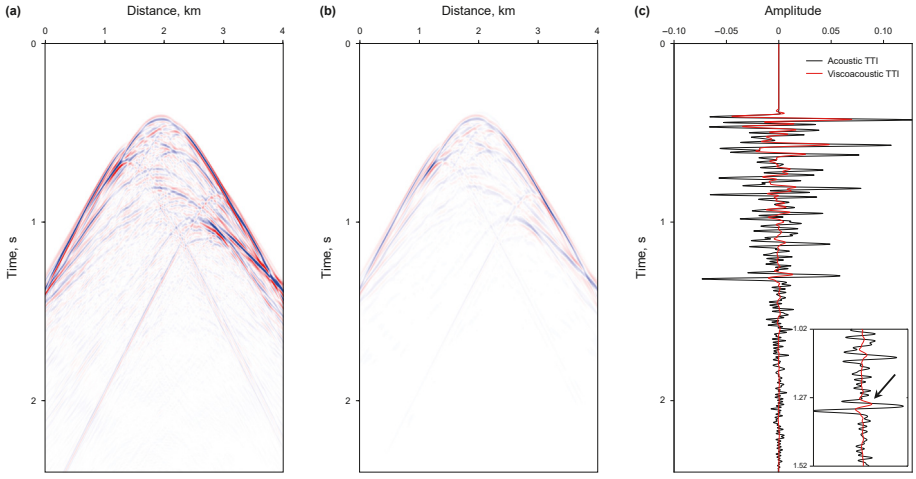

Fig. 5. Shot gathers of **(a)** acoustic TTI and **(b)** viscoacoustic TTI. **(c)** The comparison of single traces extracted from Fig. 5(a)–(b) at a distance of $x = 2$ km. Viscoacoustic TTI data exhibit obvious amplitude attenuation and phase dispersion, as compared with acoustic TTI data.

wave equation, respectively. Fig. 6(c) shows the comparison between Fig. 6(a) and (b), revealing that the traces extracted from Fig. 6(b) agree well with those extracted from Fig. 6(a). This finding indicates that the proposed wave equation accurately simulates seismic wave propagation in complex attenuating anisotropic media.

We employ the acoustic TTI RTM algorithm on the acoustic TTI data (without attenuation) to produce reference results, as shown in Fig. 7(a). Fig. 7(b) shows the uncompensated TTI RTM images obtained by conducting acoustic TTI RTM on viscoacoustic TTI data. Fig. 7(c) and (d) are Q-compensated isotropic (ISO) RTM and Q-compensated TTI RTM images, respectively. The regularization parameter is set to 0.1. Compared with the reference results (Fig. 7(a)), the amplitude of uncompensated images (Fig. 7(b)) is significantly reduced, particularly in the area below the gas chimney. In Fig. 7(c), where attenuation is compensated only using ISO parameters, the anticline events exhibit mispositioned and defocused (denoted by the white arrows). This is the impact of neglecting anisotropic effects. In comparison to Fig. 7(b)–(c), considering both the effects of anisotropy and attenuation in migration process, the imaging results in Fig. 7(d) are comparable to the reference results.

Fig. 8 depicts the single traces extracted from Fig. 7 for a clear comparison. The traces extracted from Fig. 7(a) is used as reference (denoted by the blue solid lines). Compared to the reference traces, the traces extracted from Fig. 7(b) and (c) exhibits significantly reduced amplitude and distorted events, whereas the traces extracted from Fig. 7(d) agree well with the reference results. The above results suggest that the proposed Q-compensated TTI RTM can simultaneously correct for effects of anisotropy and attenuation, providing accurate imaging results.

3.2. Complex marmousi TTI model

The modified attenuating Marmousi TTI model is further used to illustrate the adaptability of the proposed Q-compensated TTI RTM. Fig. 9 shows the model parameters of Marmousi TTI model, discretized into 601 × 251 grids with a space interval of 12.5 m in the x- and z-directions. We excite 100 shots uniformly across the surface at a shot depth of 12.5 m. Each shot has 601 receivers for recording reflections. The source is a Ricker wavelet with a dominant frequency of 20 Hz, the time step is 0.0008 s, and the total record time is 4 s.

Fig. 10(a) shows the imaging results of acoustic TTI RTM using the acoustic TTI data, used as the reference. Fig. 10(b)–(d) depict the imaging results obtained by conducting acoustic TTI RTM, Q-

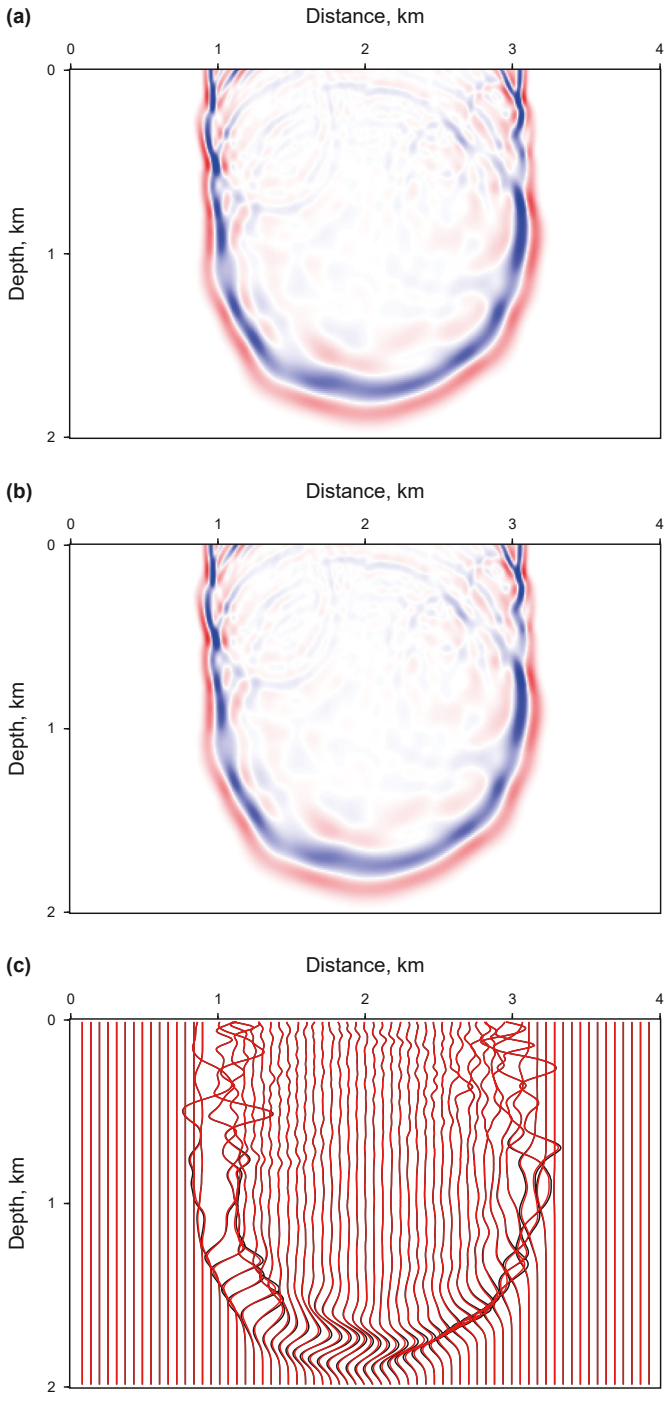

Fig. 6. Wavefield snapshots at 0.8 s in BP gas chimney TTI model simulated by the different wave equations. **(a)** and **(b)** are simulated by the coupled pseudo-viscoacoustic TTI wave equation and the proposed pure-viscoacoustic TTI wave equation, respectively. **(c)** The superposition of Fig. 6(a) (black solid line) and Fig. 6(b) (red solid line). All snapshots are plotted in the same color scale.

compensated ISO RTM and *Q*-compensated TTI RTM on viscoacoustic TTI data, respectively. The regularization parameter is set to 0.12. In Fig. 10(b), compared with the reference (Fig. 10(a)), it is evident that the imaging results has the weak energy, particularly in region below the strong attenuation structure, attributed to the absence of compensation during the migration process. However, when employing the ISO parameters for compensation, the imaging results in Fig. 10(c) exhibit the dislocation of geological structure and the distorted fault planes, highlighting the significance of anisotropic effects. Considering both anisotropy and attenuation during the migration process, the amplitude of images is consistent with that of the reference images (Fig. 10(a)) and the location of the geological structure is accurately imaged, as shown in Fig. 10(d).

For a clear comparison, we also extract the vertical slices from Fig. 10 and present them in Fig. 11. As shown in Fig. 11, in comparison to the reference traces (denoted by the blue solid lines), the traces extracted from Fig. 10(b)–(c) exhibit obvious attenuated amplitude and shifted phase. However, the traces (denoted by the red dashed lines) extracted from *Q*-compensated TTI RTM images are in good agreement with the reference traces. This example suggests that the proposed *Q*-compensated TTI RTM can provide high-quality imaging results in complex attenuating anisotropic media.

Additionally, we also test our *Q*-compensated TTI RTM algorithm with noisy data. The noisy data is obtained by adding Gaussian random noise with a frequency band of 0–500 Hz to the viscoacoustic TTI data, with the signal to noise ratio (SNR) of 10 dB. Fig. 12(a) shows a comparison between the noisy data (red lines) and the noisy-free data (black lines). The *Q*-compensated TTI RTM imaging result using the noisy data is shown in Fig. 12(b). Fig. 12(b) illustrates that the proposed *Q*-compensated TTI RTM algorithm can preserve the geologic structure despite the strong noise, indicating its stability with noisy data.

3.3. Field data test

Finally, we apply the proposed *Q*-compensated TTI RTM approach on the field data to illustrate its efficacy in attenuating TTI media. The field data consist of 204 shot gathers with a shot interval of 50 m. For each shot, there are 60 receivers with a receiver interval of 50 m. The total record length is 3.6 s with a time increment of 0.0006 s. A Ricker wavelet with a peak frequency of 35 Hz is used as source. Fig. 13 shows the migration models provided by the oil field department, and are discretized into the grid of 1185 × 635 with a spatial step of 10 m in the *x*- and *z*-directions.

Fig. 14(a) shows the imaging results obtained through acoustic RTM. Although most of the shallow reflectors are well-imaged, the deep-layers exhibit mispositioning and weak amplitudes. Fig. 14(b) and (c) present results of *Q*-compensated ISO RTM and acoustic TTI RTM applied to field data, respectively. Compared with Fig. 14(a) , (b) exhibits obvious enhanced amplitude (denoted by the black solid arrows), and Fig. 14(c) displays more continuous reflectors (denoted by the black solid arrows). The regularization parameter is set to 0.05. Fig. 14(d) shows images from *Q*-compensated TTI RTM, revealing more continuous seismic events, clearer fault planes, and effective compensation of deep geologic structures compared to Fig. 14(a)–(c).

Furthermore, Fig. 15 depicts the enlarged results of the dashed white boxes shown in Fig. 14. It is evident in Fig. 15(b) that there is enhanced amplitude, emphasizing the importance of compensating for attenuation. The images in Fig. 15(c) exhibit continuous seismic events and clear fault lines (denoted by white arrows), highlighting the significance of anisotropy correction. In comparison to Fig. 15(a)–(c), Fig. 15(d) effectively compensates for energy in deep layers, resulting in more continuous reflectors and clearer fault characterization (indicated by the white arrows). This result suggests that simultaneous correction of the anisotropy and attenuation effects of underground media is critical for improving the quality of seismic imaging. Additionally, we also generate the wavenumber spectra of Fig. 15(a)–(d), as shown in Fig. 16. Fig. 16 shows that the wavenumber spectra of imaging results obtained using *Q*-compensated TTI RTM (red lines) has the widened

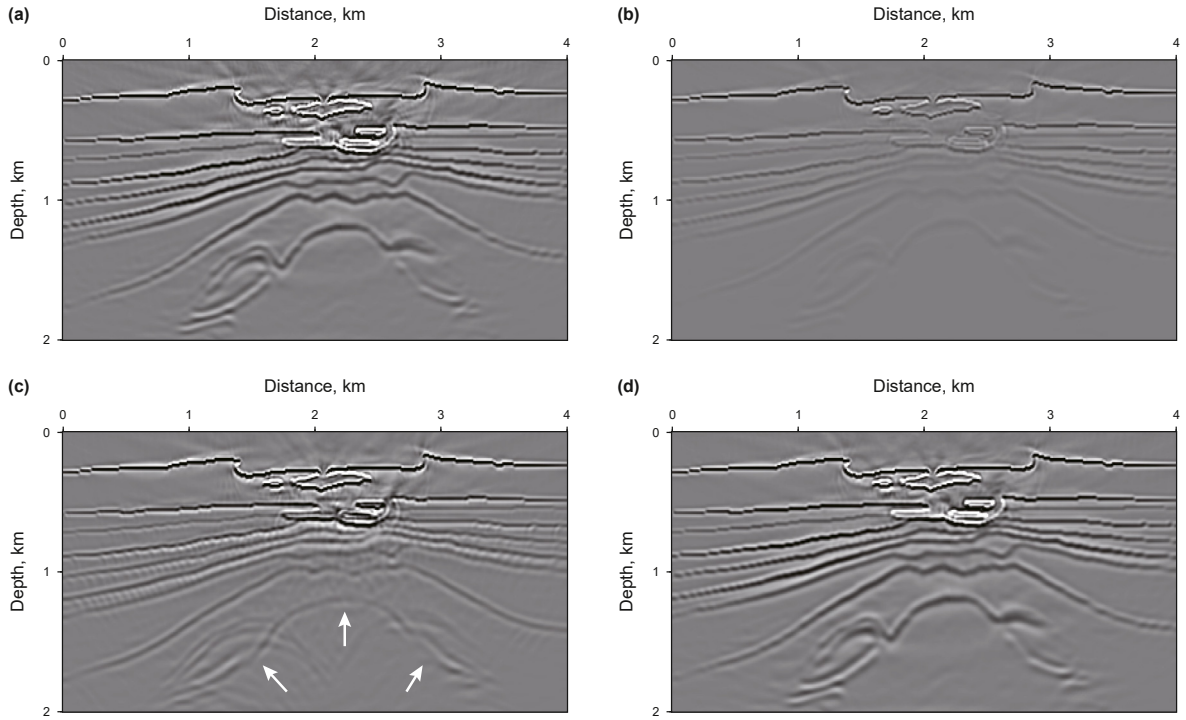

Fig. 7. Migration results for the BP gas chimney TTI model: **(a)** acoustic TTI RTM using acoustic TTI data (reference), **(b)** acoustic TTI RTM using viscoacoustic TTI data (TTI RTM), **(c)** acoustic isotropic *Q*-compensated RTM using viscoacoustic TTI data (ISO *Q*-RTM), **(d)** viscoacoustic *Q*-compensated TTI RTM using viscoacoustic TTI data (TTI *Q*-RTM). All images are plotted in the same color scale.

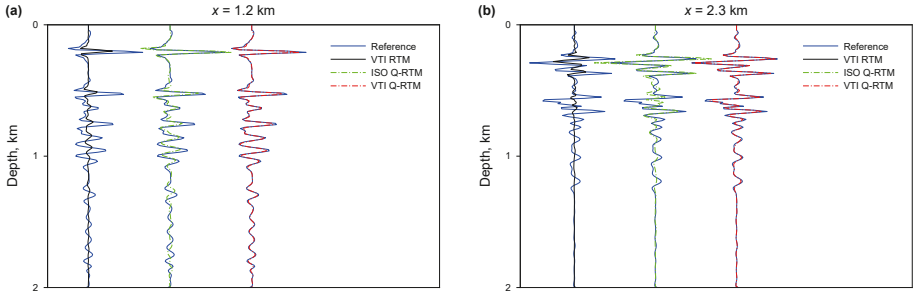

Fig. 8. The comparison of vertical slices extracted from Fig. 7 at a distance of $x = 1$ km **(a)** and $x = 2$ km **(b)**. The blue solid lines, the black solid lines, the green dashed lines, and the red dashed lines denote the traces extracted from Fig. 7(a), (b), (c), and (d), respectively.

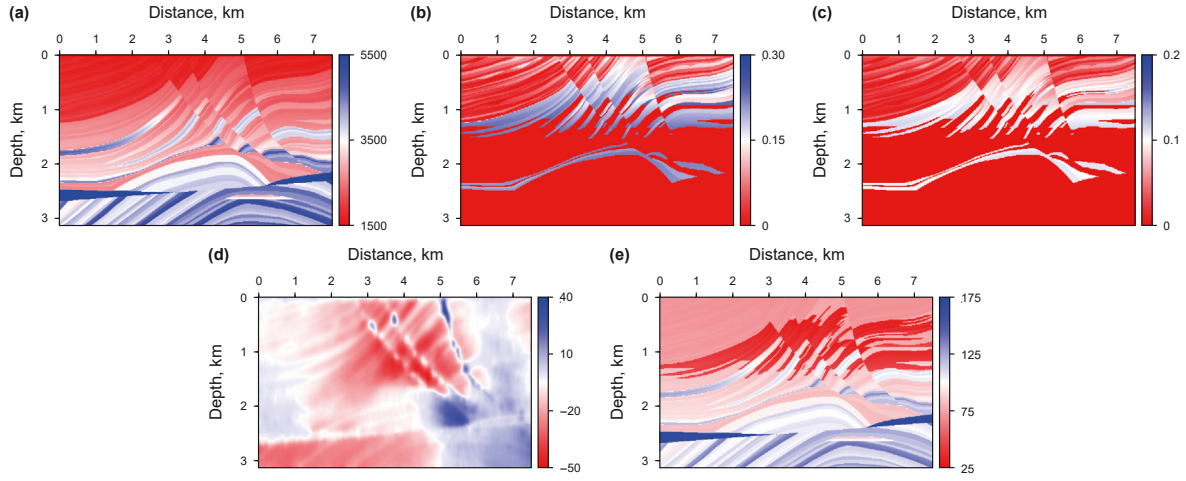

Fig. 9. The model parameters of Marmousi attenuating TTI model: **(a)** velocity model, **(b)** ε model, **(c)** δ model, **(d)** θ model, and **(e)** Q model.

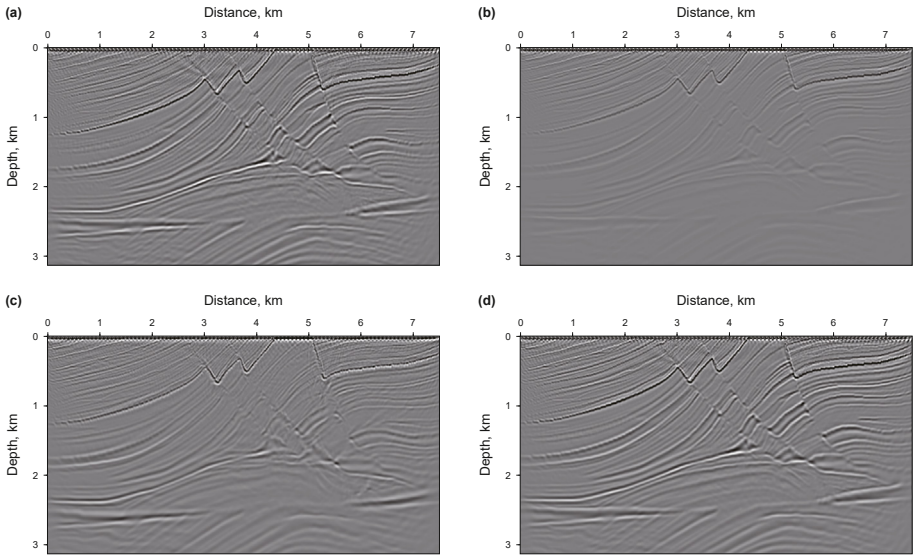

Fig. 10. Migration results for the Marmousi attenuating TTI model: **(a)** acoustic TTI RTM using acoustic TTI data (reference), **(b)** acoustic TTI RTM using viscoacoustic TTI data (TTI RTM), **(c)** acoustic isotropic *Q*-compensated RTM using viscoacoustic TTI data (ISO *Q*-RTM), **(d)** viscoacoustic *Q*-compensated TTI RTM using viscoacoustic TTI data (TTI *Q*-RTM). All images share the same color scale.

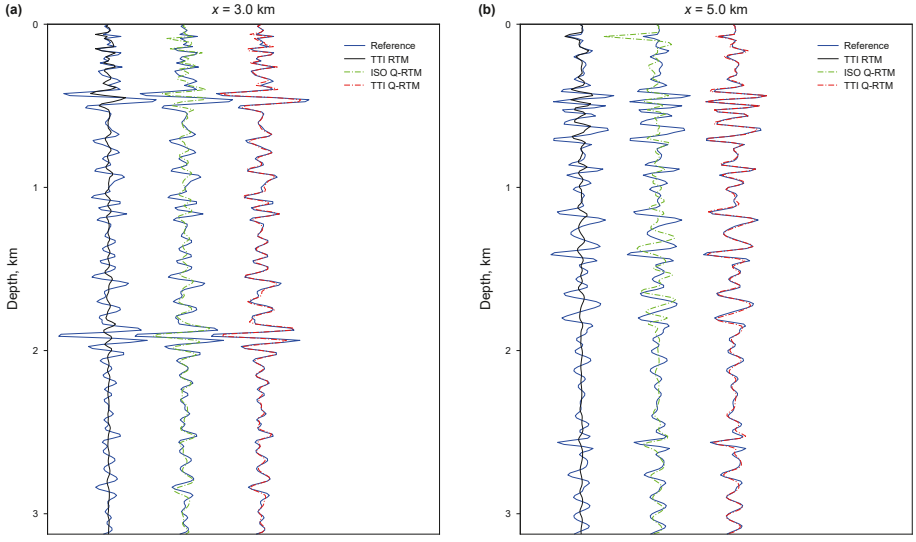

Fig. 11. The comparison of vertical slices extracted from Fig. 10 at a distance of $x = 3.0$ km **(a)** and $x = 5.0$ km **(b)**. The blue solid lines, the black solid lines, the green dashed lines, and the red dashed lines denote the traces extracted from Fig. 10(a), (b), (c), and (d), respectively.

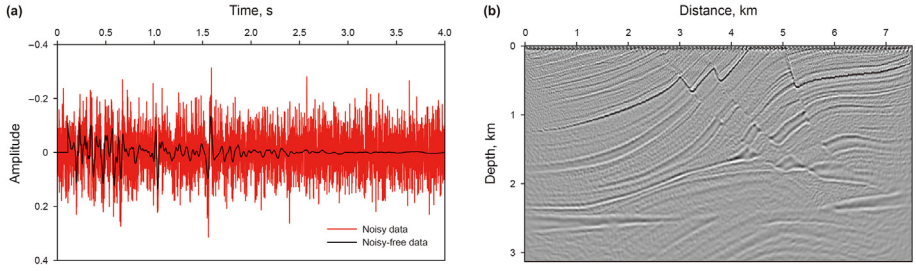

Fig. 12. Migration results for the Marmousi attenuating TTI model with noisy data. **(a)** The comparison of noisy-free data (black lines) and noisy data (red lines), with a signal-to-noise ratio (SNR) of 10 dB. **(b)** Viscoacoustic *Q*-compensated TTI RTM images using the noisy data.

frequency bands and improved imaging resolution. This illustrates that the proposed *Q*-compensated TTI RTM scheme can enhance imaging quality in terms of energy and resolution compared to the non-compensated case. Therefore, we can conclude that the proposed *Q*-compensated TTI RTM effectively corrects for the attenuation and anisotropic effects simultaneously, which can be used as a

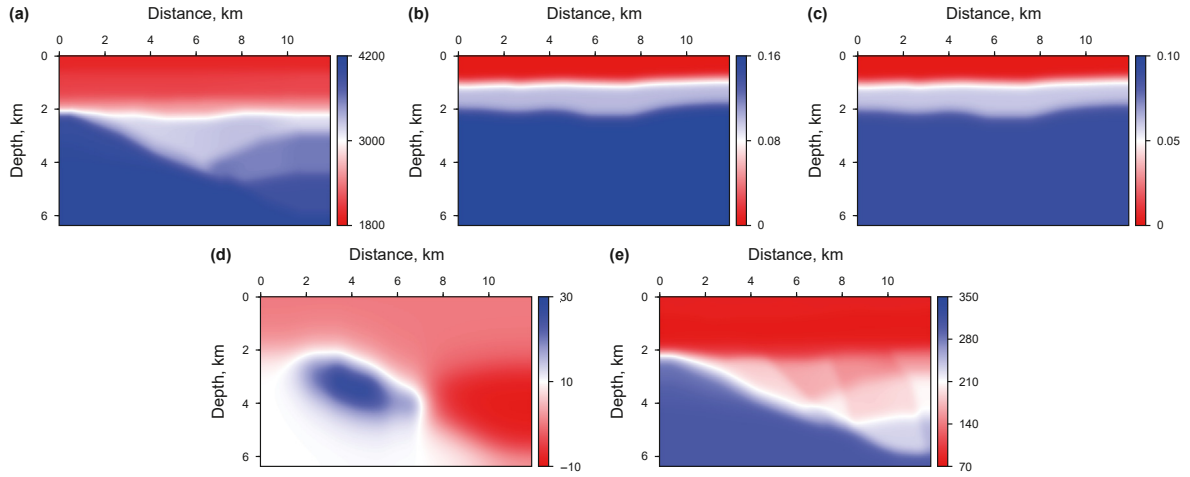

Fig. 13. The migration model of field data: **(a)** velocity model, **(b)** ε model, **(c)** δ model, **(d)** θ model, and **(e)** Q model.

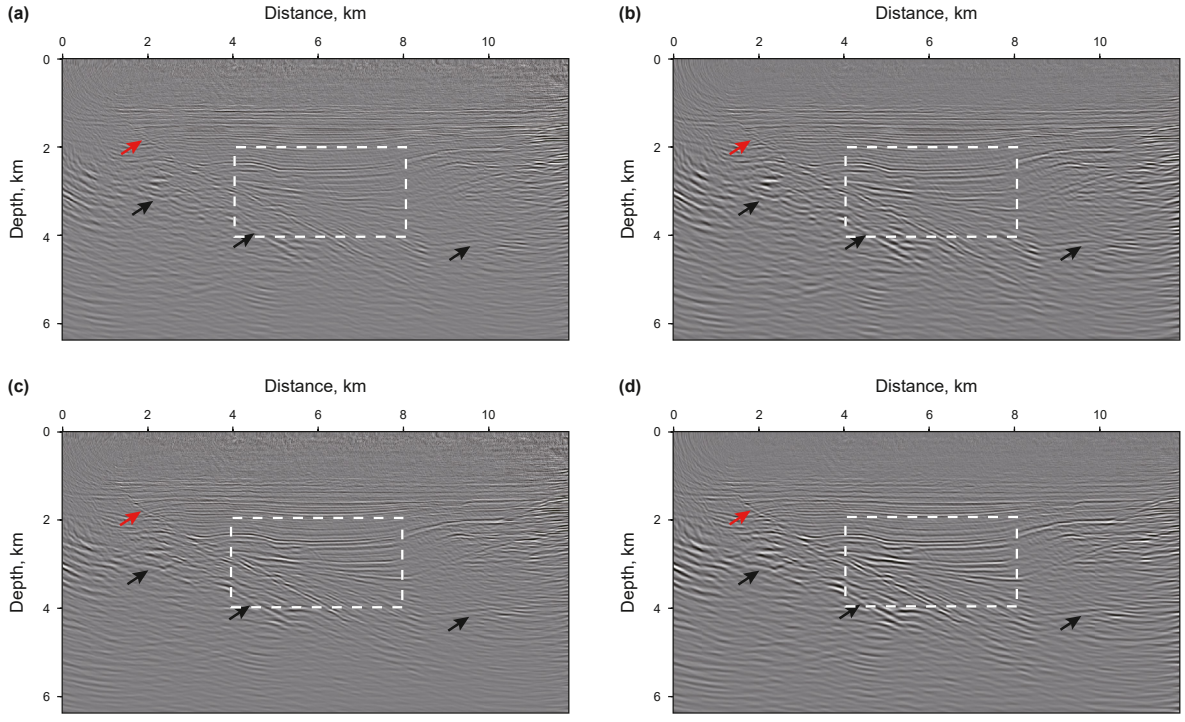

Fig. 14. Migration results for the field data using different RTM schemes: **(a)** acoustic RTM, **(b)** acoustic isotropic Q-compensated RTM (ISO Q-RTM), **(c)** acoustic TTI RTM, **(d)** viscoacoustic Q-compensated TTI RTM (TTI Q-RTM). All images share the same color scale.

reliable imaging technique for attenuating TTI media.

4. Discussion

4.1. Computational efficiency analysis of the proposed wave equation

To simulate the propagation behavior of seismic waves in attenuating TTI media, we develop a new memory-variable-expressed pure-viscoacoustic TTI wave equation. In comparison to the previous memory-variable-expressed wave equation, the newly derived wave equation with the decoupled phase dispersion and amplitude attenuation operators, facilitating the implementation of Q-compensated RTM. Over the years, a series of fractional pure-viscoacoustic TTI wave equations also are derived for simulating the seismic wave propagation in attenuating anisotropic media (Xu et al., 2015; Gu et al., 2022; Mu et al., 2022). However, these wave equations require computational expensive FFTs for solving fractional Laplacians. In contrast, the proposed pure-viscoacoustic TTI wave equation can be easily solved by the finite-difference (FD) method, which is highly efficient in attenuating TTI media.

In order to demonstrate the computational efficiency advantage of our new wave equation, we conduct a comparative analysis with pure-viscoacoustic TTI wave equations expressed using the fractional Laplacian. Drawing on the work of Gu et al. (2022), the fractional Laplacian pure-viscoacoustic TTI wave equation can be expressed as

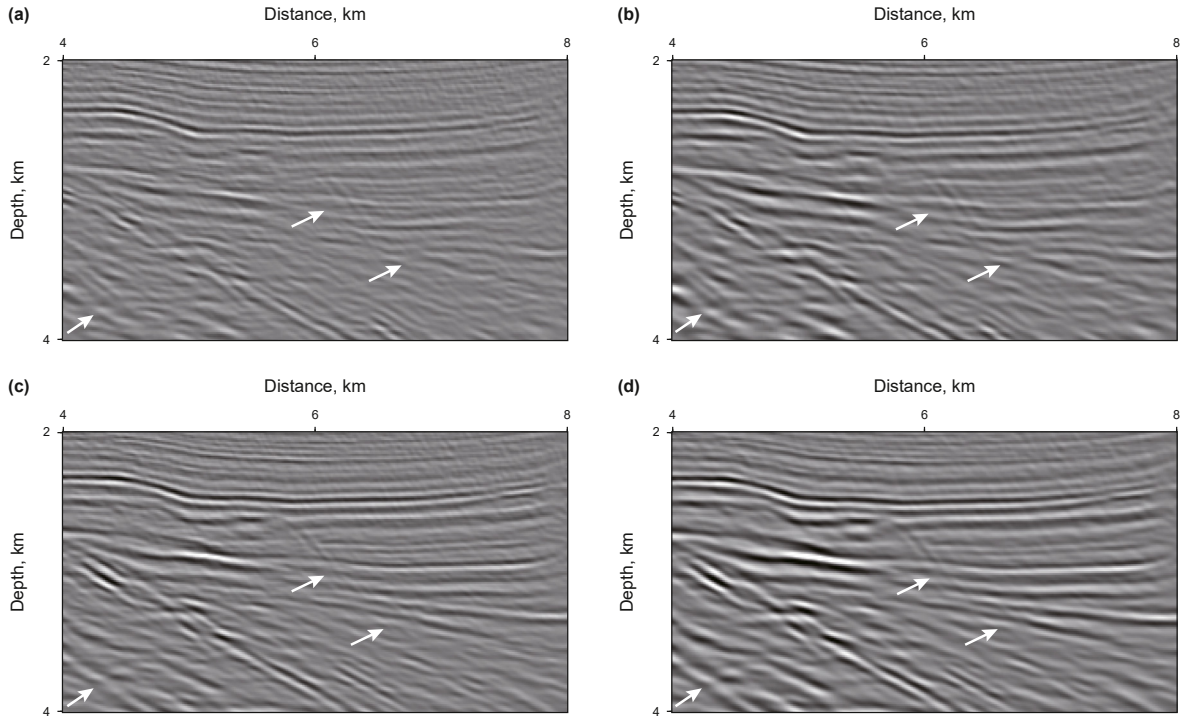

Fig. 15. The magnified results of the dashed white boxes shown in Fig. 14: **(a)** acoustic RTM, **(b)** acoustic isotropic *Q*-compensated RTM (ISO *Q*-RTM), **(c)** acoustic TTI RTM, **(d)** viscoacoustic *Q*-compensated TTI RTM (TTI *Q*-RTM).

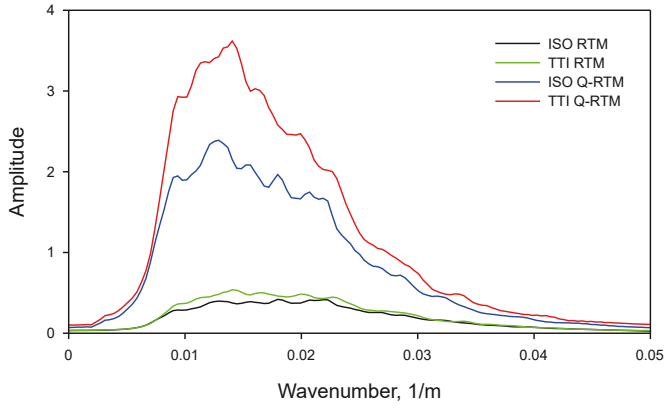

Fig. 16. The average wavenumber spectra calculated along the vertical direction for the imaging results of Fig. 15. The black solid lines, the green dashed lines, the blue solid lines, and the red dashed lines denote the wavenumber spectrum of the images in Fig. 15(a), (c), (b), and (d), respectively.

$$\frac{\partial^2 p}{\partial t^2} = v_{p0}^2\left(\eta\left(-\nabla^2\right)^{\gamma} + \tau\frac{\partial}{\partial t}\left(-\nabla^2\right)^{\gamma-1/2}\right)\left(2\varepsilon T_{xx}p + \left(\frac{\partial^2 p}{\partial x^2} + \frac{\partial^2 p}{\partial z^2}\right)(1-\bar{S}_n)\right), \tag{31}$$

$$\eta = v_{p0}^{2\gamma}\cos^2(\pi\gamma/2)\omega_0^{-2\gamma}\cos(\pi\gamma), \tau = v_{p0}^{2\gamma-1}\cos^2(\pi\gamma/2)\omega_0^{-2\gamma}\sin(\pi\gamma), \tag{32}$$

where ω_0 denotes the reference angular frequency, $\gamma = \arctan(1/Q)/\pi$, Q is quality factor. Additionally, Fathalian et al. (2020) derive a first-order viscoacoustic wave equation with the decoupled amplitude loss and phase dispersion terms, based on SLS model. According to the derivation of Fathalian et al. (2020), we derived a SLS-based pure-viscoacoustic TTI wave equation as follows (see Appendix B):

$$\frac{1}{v_{p0}^2}\frac{\partial^2 p}{\partial t^2} = \left(\frac{2}{A} + i\frac{2}{AQ}\right)\left(2\varepsilon T_{xx}p + \left(\frac{\partial^2 p}{\partial x^2} + \frac{\partial^2 p}{\partial z^2}\right)(1-\bar{S}_n)\right). \tag{33}$$

Subsequently, we perform simulations in a homogeneous model with the different grid points using the abovementioned wave equations, and the grid spacing of the model is 10 m. The model parameters are same as those in Fig. 1. Table 1 shows the computational time of the different wave equations. The computational platform is a matlab software, equipped in a computer with an Intel Core i5-10505 at 3.20 GHz processor. As illustrated in Table 1, the computational speed of the newly derived wave equation is nearly twice as fast as that of Eq. (33) and almost four times faster than Eq. (31), highlighting the high computational efficiency of our new wave equation. This is due the fact that the proposed wave equation can be easily solved by the finite-difference method. However, Eq. (32) requires at least two forward FFTs and two inverse FFTs, whereas Eq. (33) requires at least one forward FFTs and one inverse FFTs. This observation suggests that the proposed pure-viscoacoustic wave equation is highly efficient and holds great potential for practical application.

Table 1
Running time of the wavefield simulation with a duration of 3 s in homogeneous model with the different mesh sizes.

Equations	201 × 201	401 × 401	601 × 601	801 × 801
Eq. (31)	132.35 s	412.62 s	1206.45 s	2563.52 s
Eq. (33)	76.24 s	212.56 s	565.12 s	1126.37 s
Proposed	34.85 s	104.72 s	278.30 s	514.69 s

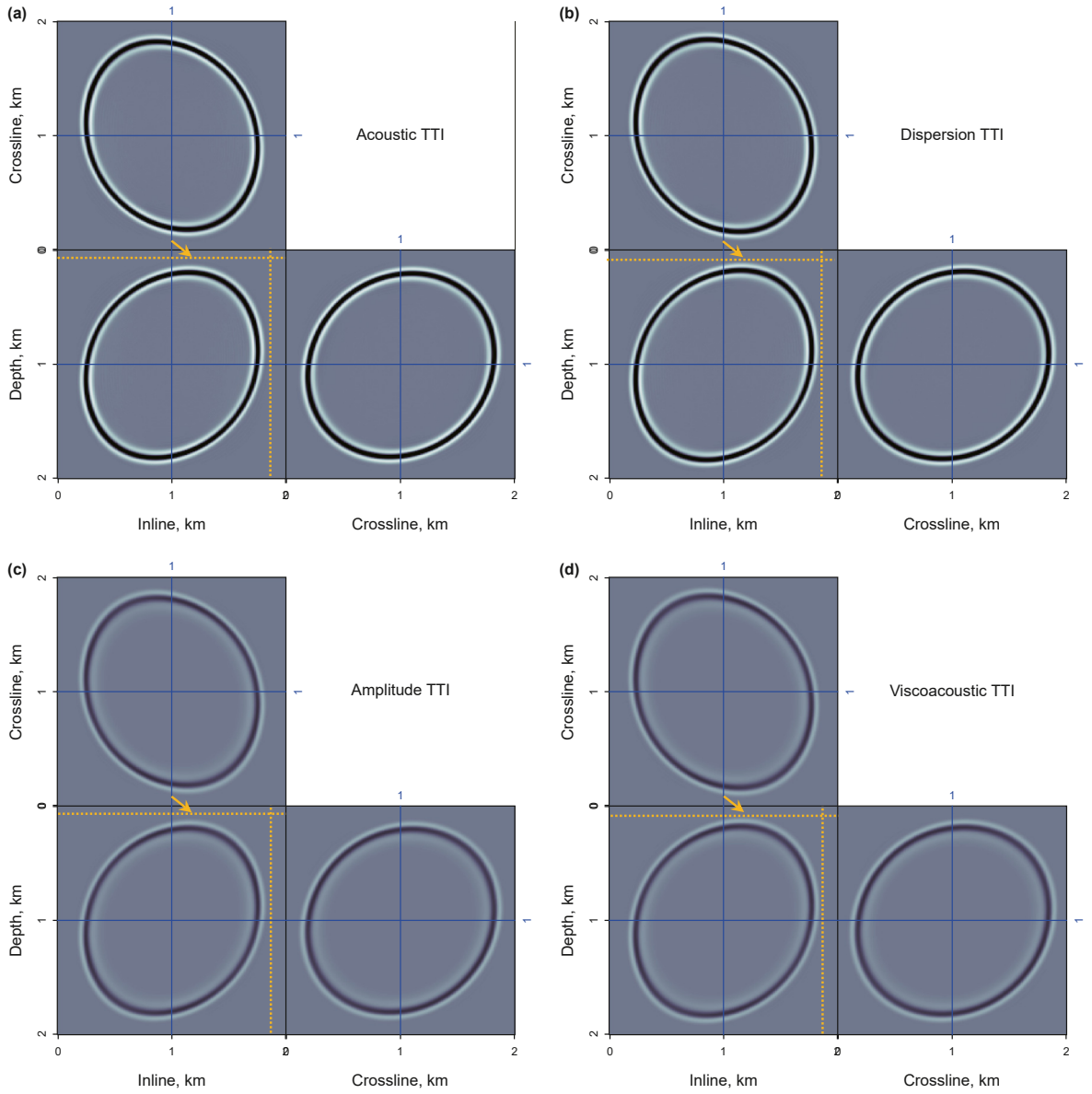

Fig. 17. Wavefield snapshots at 0.35 s for the homogeneous model: **(a)** Wavefields simulated through pure acoustic TTI wave equation. **(b)** Wavefields simulated through phase-dispersion dominated pure viscoacoustic TTI wave equation. **(c)** Wavefields simulated through amplitude-loss dominated pure viscoacoustic TTI wave equation. **(d)** Wavefields simulated through pure viscoacoustic TTI wave equation. All plots are in same color scale.

4.2. Future application of the proposed wave equation

In recent decades, the utilization of three-dimensional (3D) approaches has drawn a lot of attention in attenuating media (Shen et al., 2018b). The biggest factor restricting 3D application is computational efficiency. Additionally, the existing viscoacoustic anisotropic wave equation with the decoupled amplitude dissipation and phase dispersion terms, necessitates solving using multiple Fast Fourier Transforms (FFTs). We know that the FFTs are computational inefficient and unsuitable for the practical application, especially in 3D application. In comparison to the previous wave equations, the proposed pure-viscoacoustic TTI wave equation can be efficiently solved by the finite-difference method and can be easily extended to 3D applications.

To demonstrate the possibility of 3D application of our new wave equation, we design a homogeneous model with the grids points of 201 $\times$ 201 $\times$ 201, the spatial step is 10 m. The model parameters are $v_{p0} = 3000$ m/s, $\varepsilon = 0.25$, $\delta = 0.1$, $\theta = 60$, $\varphi = 30$, $Q = 20$. Fig. 17 shows the wavefields simulated by the different wave equations. The acoustic TTI wavefields shown in Fig. 17(a) are used as reference. Compared with Fig. 17(a), the phase-dispersion wavefields ($\kappa_1 = 1$ and $\kappa_2 = 0$) show noticeable phase delay, while the amplitude-loss wavefields ($\kappa_1 = 0$ and $\kappa_2 = 1$) exhibit reduced amplitude. Fig. 17(d) are wavefields simulated by the proposed pure-viscoacoustic TTI wave equation, showing evident phase delay and reduced amplitude, compared to Fig. 17(a). This finding suggests that the proposed 3D pure-viscoacoustic TTI wave equation is capable of simulating amplitude attenuation and phase dispersion effects separately. This is conducive for the realization of 3D Q-compensated RTM. As a result, the 3D Q-compensated RTM and 3D Q-compensated least-squares RTM based on the proposed wave equation is the future work of this paper.

Additionally, there has been significant attention given to Q-related full waveform inversion (FWI) (Shen et al., 2018b; Da Silva

et al., 2019b; Yang et al., 2016). Over the years, Q-related FWI typically relied on the fractional Laplacians expressed viscoacoustic wave equation (Xing and Zhu, 2023). As discussed above, the computational efficiency of the fractional Laplacians expressed viscoacoustic anisotropic wave equation is unsatisfactory. On the contrary, the newly derived wave equation can be solved by the FD method, enhances the calculation speed of Q-related FWI during inversion, rendering it suitable for FWI applications. Additionally, the decoupling of amplitude dissipation and phase dispersion of the proposed wave equation can help compensating the gradient of Q-related FWI (Xing and Zhu, 2023), thereby accelerating the convergence speed. Given these advantages, our new wave equation is well-suited for Q-related FWI. Therefore, integrating the proposed wave equation into Q-related FWI is another aspect of our future work.

5. Conclusion

We propose a highly efficient pure-viscoacoustic Q-compensated reverse time migration (RTM) algorithm in tilted transversely isotropic (TTI) media. To implement Q-compensated TTI RTM, we derive a memory-variable expressed pure-viscoacoustic TTI wave equation with decoupled amplitude dissipation and phase dispersion term. In comparison to the previous pure-viscoacoustic TTI wave equation, the newly derived pure-viscoacoustic TTI wave equation can be efficiently solved by the finite-difference method and is well-suited for industrial applications. Numerical tests show that the proposed pure-viscoacoustic TTI wave equation can simulate the behavior of amplitude loss and phase dispersion separately, providing S-wave artifact-free and numerically stable wavefields. Building on the newly derived wave equation, we develop the Q-compensated RTM algorithm in TTI media. To suppress the high-frequency noise in wavefields, a regularization operator is incorporated into the attenuation-compensated wavefields modeling operator, ensuring the stable propagation of wavefields. Synthetic examples and field data test suggest that the proposed Q-compensated TTI RTM technique can effectively correct for the effects of anisotropy and attenuation, resulting in the high-resolution imaging results. Furthermore, the proposed wave equation can be well used as forward engine for full waveform inversion in attenuating TTI media.

CRediT authorship contribution statement

Qiang Mao: Writing – original draft, Validation, Software, Resources, Methodology, Investigation, Data curation, Conceptualization. **Jian-Ping Huang:** Writing – review & editing, Supervision, Resources, Funding acquisition. **Xin-Ru Mu:** Visualization, Investigation, Conceptualization. **Yu-Jian Zhang:** Formal analysis, Data curation.

Declaration of competing interest

All authors certify that they have no affiliations with or involvement in any organization or entity with any financial interest or non-financial interest in the subject matter or materials discussed in this manuscript.

Acknowledgements

We thank the editors and two anonymous reviewers for their insightful comments that significantly improved the quality of this paper. This study is supported by the Marine S&T Fund of Shandong Province for Pilot National Laboratory for Marine Science and Technology (Qingdao) (No. 2021QNLM020001), the Major Scientific and Technological Projects of Shandong Energy Group (No. SNKJ2022A06-R23), the National Natural Science Foundation of China (No. 42374164), and the basic theoretical research of seismic wave imaging technology in complex oilfield of Changqing Oilfield Company (No. 2023-10502).

Appendix A

The pure-viscoacoustic wave equation in 3D tilted transversely isotropic media.

According to Eq. (19), the 3D version of the newly derived pure-viscoacoustic TTI wave equation can be written as

$$\frac{\partial^2 p}{\partial t^2}=v_{p0}^2\left\{\left(2\varepsilon(T_{xx}+T_{yy})p+\left(\frac{\partial^2 p}{\partial x^2}+\frac{\partial^2 p}{\partial y^2}+\frac{\partial^2 p}{\partial z^2}\right)(1-\bar{S}_n)\right)\frac{\tau_\varepsilon}{\tau_\sigma}-r\right\}, \tag{A-1}$$

$$\frac{\partial r}{\partial t}=-\frac{1}{\tau_\sigma}\left\{r-\left(\frac{\tau_\varepsilon}{\tau_\sigma}-1\right)\left(2\varepsilon(T_{xx}+T_{yy})p+\left(\frac{\partial^2 p}{\partial x^2}+\frac{\partial^2 p}{\partial y^2}+\frac{\partial^2 p}{\partial z^2}\right)(1-\bar{S}_n)\right)\right\}, \tag{A-2}$$

where

$$\bar{S}_n\approx\frac{2(\varepsilon-\delta)\left(T_x^2+T_y^2\right)\Big/T_z^2}{1+(1+2\varepsilon)\left[\left(T_x^2+T_y^2\right)\Big/T_z^2\right]^2+(2+2\delta)\left(T_x^2+T_y^2\right)\Big/T_z^2}, \tag{A-3}$$

$$T_{xx}=\cos^2(\theta)\cos^2(\varphi)\frac{\partial^2}{\partial x^2}+\cos^2(\theta)\sin^2(\varphi)\frac{\partial^2}{\partial y^2}+\cos^2(\theta)\sin(2\varphi)\frac{\partial^2}{\partial x\partial y}+\sin^2(\theta)\frac{\partial^2}{\partial z^2}-\sin(2\theta)\cos(\varphi)\frac{\partial^2}{\partial x\partial z}-\sin(2\theta)\sin(\varphi)\frac{\partial^2}{\partial y\partial z}, \tag{A-4}$$

$$T_{yy}=\sin^2(\varphi)\frac{\partial^2}{\partial x^2}-\sin(2\varphi)\frac{\partial^2}{\partial x\partial y}+\cos^2(\varphi)\frac{\partial^2}{\partial y^2}. \tag{A-5}$$

$$\begin{aligned}T_x&=\cos(\theta)\cos(\varphi)\frac{\partial}{\partial x}+\cos(\theta)\sin(\varphi)\frac{\partial}{\partial y}-\sin(\theta)\frac{\partial}{\partial z},\\ T_y&=-\sin(\varphi)\frac{\partial}{\partial x}+\cos(\varphi)\frac{\partial}{\partial y},\\ T_z&=\sin(\theta)\cos(\varphi)\frac{\partial}{\partial x}+\sin(\theta)\sin(\varphi)\frac{\partial}{\partial y}+\cos(\theta)\frac{\partial}{\partial z}.\end{aligned} \tag{A-6}$$

Similar to the derivation of Eq. (25), Eq. (A-1) can be written as

$$\frac{1}{v_{p0}^2}\frac{\partial^2 p}{\partial t^2}=\left(2\varepsilon(T_{xx}+T_{yy})p+\left(\frac{\partial^2 p}{\partial x^2}+\frac{\partial^2 p}{\partial y^2}+\frac{\partial^2 p}{\partial z^2}\right)(1-\bar{S}_n)\right)\left(1+\kappa_1\left(\frac{2}{A}-1\right)+\kappa_2\left[\frac{\tau_\varepsilon}{\tau_\sigma}-\frac{2}{A}\right]\right)-\kappa_2 r, \tag{A-7}$$

where κ_1 and κ_2 are the constant. $\kappa_1=0$ and $\kappa_2=0$, Eq. (A-7) becomes acoustic anisotropic wave equation derived in Liang et al. (2023); $\kappa_1=1$ and $\kappa_2=0$, Eq. (A-7) becomes dispersion-

dominated pure-viscoacoustic TTI wave equation; $\kappa_1 = 0$ and $\kappa_2 = 1$, Eq. (A-7) becomes amplitude-dominated pure-viscoacoustic TTI wave equation; $\kappa_1 = 1$ and $\kappa_2 = 1$, Eq. (A-7) becomes pure-viscoacoustic TTI wave equation.

Appendix B

Derivation of phase dispersion dominated pure-viscoacoustic TTI wave equation.

From Eq. (9), we can calculate the memory variable associated with the relaxation time:

$$\tilde{r} = \Big\{(1+2\varepsilon) \times \Big(k_x^2+k_y^2\Big)P + k_z^2 P - S_k\Big(k_x^2+k_y^2+k_z^2\Big)P\Big\}\frac{\tau_\sigma^{-1}(1-\tau_\varepsilon\tau_\sigma^{-1})}{(i\omega+\tau_\sigma^{-1})}. \tag{B-1}$$

Substituting Eq. (B-1) into Eq. (8), Eq. (8) can be rewritten as

$$\omega^2 P = v_{p0}^2\left\{\Big\{(1+2\varepsilon)\Big(k_x^2+k_y^2\Big)P + k_z^2P - S_k\Big(k_x^2+k_y^2+k_z^2\Big)P\Big\} \times\left[\frac{\tau_\varepsilon}{\tau_\sigma}+\frac{\tau_\sigma^{-1}(1-\tau_\varepsilon\tau_\sigma^{-1})}{(i\omega+\tau_\sigma^{-1})}\right]\right\}. \tag{B-2}$$

According to the derivation of Fathalian et al. (2020), we have

$$\frac{\tau_\varepsilon}{\tau_\sigma}+\frac{\tau_\sigma^{-1}(1-\tau_\varepsilon\tau_\sigma^{-1})}{(i\omega+\tau_\sigma^{-1})} = \frac{i\omega\tau_\varepsilon\tau_\sigma^{-1}+\tau_\sigma^{-1}}{(i\omega+\tau_\sigma^{-1})} = \frac{i\omega\tau_\varepsilon\tau_\sigma^{-1}+\tau_\sigma^{-1}}{(i\omega+\tau_\sigma^{-1})} \times\frac{(-i\omega+\tau_\sigma^{-1})}{(-i\omega+\tau_\sigma^{-1})} = \frac{\omega^2\tau_\varepsilon\tau_\sigma+1}{1+\omega^2\tau_\sigma^2}+i\frac{\omega(\tau_\varepsilon-\tau_\sigma)}{1+\omega^2\tau_\sigma^2} = \frac{2}{A}+i\frac{2}{AQ}, \tag{B-3}$$

where $A = 1+(\sqrt{1+1/Q^2}-1/Q)^2$. By inserting Eq. (B-3) into Eq. (B-2), Eq. (B-2) can be expressed as

$$\omega^2 P = v_{p0}^2\left\{\Big\{(1+2\varepsilon)\Big(k_x^2+k_y^2\Big)P + k_z^2P - S_k\Big(k_x^2+k_y^2+k_z^2\Big)P\Big\}\left[\frac{2}{A}+i\frac{2}{AQ}\right]\right\}, \tag{B-4}$$

where the terms associated with $2/A$ and $2/AQ$ are related to phase dispersion and amplitude loss, respectively. Transforming Eq. (B-4) into the time-space domain, yielding the pure-viscoacoustic TTI wave equation in the time-space domain:

$$\frac{1}{v_{p0}^2}\frac{\partial^2 p}{\partial t^2} = \left(\frac{2}{A}+i\frac{2}{AQ}\right)\left(2\varepsilon T_{xx}p+\left(\frac{\partial^2 p}{\partial x^2}+\frac{\partial^2 p}{\partial z^2}\right)(1-\bar{S}_n)\right). \tag{B-5}$$

Additionally, the phase dispersion dominated pure-viscoacoustic TTI wave equation can be expressed as

$$\frac{\partial^2 p}{\partial t^2} = v_{p0}^2\left(2\varepsilon T_{xx}p+\left(\frac{\partial^2 p}{\partial x^2}+\frac{\partial^2 p}{\partial z^2}\right)(1-\bar{S}_n)\right)\left(1+\frac{2}{A}-1\right). \tag{B-6}$$

Appendix C

The pseudo-viscoacoustic wave equation in 3D tilted transversely isotropic media.

As per the works of Fathalian et al. (2021), by selecting the single-SLS element, the second-order coupled pseudo-viscoacoustic TTI wave equation can be rewritten as

$$\frac{1}{v_{p0}^2}\frac{\partial^2 p}{\partial t^2} = \frac{\tau_\varepsilon}{\tau_\sigma}\left[(1+2\varepsilon)H_2 p+\sqrt{1+2\delta}\,H_1 q\right]-r_p, \tag{C-1}$$

$$\frac{1}{v_{p0}^2}\frac{\partial^2 q}{\partial t^2} = \frac{\tau_\varepsilon}{\tau_\sigma}\left[\sqrt{1+2\delta}\,H_2 p+H_1 q\right]-r_q, \tag{C-2}$$

$$\frac{\partial r_p}{\partial t} = -\frac{1}{\tau_\sigma}\left\{r_p-\left(\frac{\tau_\varepsilon}{\tau_\sigma}-1\right)\left[(1+2\varepsilon)H_2 p+\sqrt{1+2\delta}\,H_1 q\right]\right\}, \tag{C-3}$$

$$\frac{\partial r_q}{\partial t} = -\frac{1}{\tau_\sigma}\left\{r_q-\left(\frac{\tau_\varepsilon}{\tau_\sigma}-1\right)\left[\sqrt{1+2\delta}\,H_2 p+H_1 q\right]\right\}, \tag{C-4}$$

$$H_1 = \sin^2(\theta)\cos^2(\varphi)\frac{\partial^2}{\partial x^2}+\sin^2(\theta)\sin^2(\varphi)\frac{\partial^2}{\partial y^2}+\sin^2(\theta)\sin(2\varphi)\frac{\partial^2}{\partial x\partial y} +\cos^2(\theta)\frac{\partial^2}{\partial z^2}+\sin(2\theta)\cos(\varphi)\frac{\partial^2}{\partial x\partial z}+\sin(2\theta)\sin(\varphi)\frac{\partial^2}{\partial y\partial z}, \tag{C-5}$$

$$H_2 = \frac{\partial^2}{\partial x^2}+\frac{\partial^2}{\partial y^2}+\frac{\partial^2}{\partial z^2}-H_1, \tag{C-6}$$

where τ_σ and τ_ε stand for the stress and strain relaxation times, respectively. r_p and r_q denote the corresponding memory variable.

References

Aki, K., Richards, P., 1980. Quantitative Seismology: Theory and Methods. Freeman, San Francisco, CA. https://doi.org/10.1121/1.385057.

Alkhalifah, T., 2000. An acoustic wave equation for anisotropic media. Geophysics 65 (4), 1239–1250. https://doi.org/10.1190/1.1444815.

Bai, T., Tsvankin, I., 2016. Time-domain finite-difference modeling for attenuative anisotropic media. Geophysics 81 (2), C69–C77. https://doi.org/10.1190/geo2015-0424.1.

Best, A.I., Sothcott, J., McCann, C., 2007. A laboratory study of seismic velocity and attenuation anisotropy in near-surface sedimentary rocks. Geophys. Prospect. 55 (5), 609–625. https://doi.org/10.1111/j.1365-2478.2007.00642.x.

Blanch, J.O., Robertsson, J.O., Symes, W.W., 1995. Modeling of a constant q; methodology and algorithm for an efficient and optimally inexpensive viscoelastic technique. Geophysics 60 (1), 176–184. https://doi.org/10.1190/1.1443744.

Carcione, J.M., 1992. Anisotropic Q and velocity dispersion of finely layered media. Geophys. Prospect. 40 (7), 761–783. https://doi.org/10.1111/j.1365-2478.1992.tb00551.x.

Carcione, J.M., Cavallini, F., Mainardi, F., et al., 2002. Time-domain seismic modeling of constant Q wave propagation using fractional derivatives. Pure. Appl. Geophys. 159 (7), 1719–1736. https://doi.org/10.1007/s00024-002-8705-z.

Carcione, J.M., Kosloff, D., Kosloff, R., 1988. Wave propagation simulation in a linear viscoacoustic medium. Geophys. J. Int. 93 (2), 393–401. https://doi.org/10.1111/j.1365-246X.1988.tb02010.x.

Cerjan, C., Kosloff, D., Kosloff, R., et al., 1985. A nonreflecting boundary condition for discrete acoustic and elastic wave equations. Geophysics 50 (4), 705–708. https://doi.org/10.1190/1.1441945.

Chen, H., Zhou, H., Li, Y., 2014. Application of unsplit convolutional perfectly matched layer for scalar arbitrarily wide-angle wave equation. Geophysics 79 (6), T313–T321. https://doi.org/10.1190/geo2014-0103.1.

Chen, H., Zhou, H., Li, Q., et al., 2016. Two efficient modeling schemes for fractional Laplacian viscoacoustic wave equation. Geophysics 81 (5), T233–T249. https://doi.org/10.1190/geo2015-0660.1.

Cheng, J., Fomel, S., 2014. Fast algorithms for elastic-wave-mode separation and vector decomposition using low-rank approximation for anisotropic media.

Geophysics 79 (4), C97–C110. https://doi.org/10.1190/geo2014-0032.1.
Chu, C., Macy, B.K., Anno, P.D., 2011. Approximation of pure acoustic seismic wave propagation in TTI media. Geophysics 76 (5), WB97–WB107. https://doi.org/10.1190/geo2011-0092.1.
Da Silva, N.V., Yao, G., Warner, M., 2019a. Wave modeling in viscoacoustic media with transverse isotropy. Geophysics 84 (1), C41–C56. https://doi.org/10.1190/geo2017-0695.1.
Da Silva, N.V., Yao, G., Warner, M., 2019b. Semiglobal viscoacoustic full-waveform inversion. Geophysics 84 (2), R271–R293. https://doi.org/10.1190/geo2017-0773.1.
Dutta, G., Schuster, G.T., 2014. Attenuation compensation for least squares reverse time migration using the viscoacoustic-wave equation. Geophysics 79 (6), S251–S262. https://doi.org/10.1190/geo2013-0414.1.
Duveneck, E., Bakker, P.M., 2011. Stable P-wave modeling for reverse time migration in tilted TI media. Geophysics 76 (2), S65–S75. https://doi.org/10.1190/1.3533964.
Emmerich, H., Korn, M., 1987. Incorporation of attenuation into time domain computations of seismic wave fields. Geophysics 52 (2), 1252–1264. https://doi.org/10.1190/1.1442386.
Fathalian, A., Trad, D.O., Innanen, K.A., 2020. An approach for attenuation-compensating multidimensional constant-Q viscoacoustic reverse time migration. Geophysics 85 (1), S33–S46. https://doi.org/10.1190/geo2019-0107.1.
Fathalian, A., Trad, D.O., Innanen, K.A., 2021. Q-compensated reverse time migration in tilted transversely isotropic media. Geophysics 86 (1), S73–S89. https://doi.org/10.1190/geo2019-0466.1.
Fletcher, R., Du, X., Fowler, P., 2009. Reverse-time migration in tilted transversely isotropic (TTI) media. Geophysics 74 (6), WCA179–WCA187. https://doi.org/10.1190/1.3269902.
Grechka, V., Zhang, L., Rector III, J.W., 2004. Shear waves in acoustic anisotropic media. Geophysics 69 (2), 576–582. https://doi.org/10.1190/1.1707077.
Gu, B., Zhang, S., Duan, P., et al., 2022. Viscoacoustic wave equation for qP-wave in transversely isotropic media. J. Appl. Geophys. 203, 104681. https://doi.org/10.1016/j.jappgeo.2022.104681.
Guo, P., McMechan, G.A., Guan, H., 2016. Comparison of two viscoacoustic propagators for Q-compensated reverse time migration. Geophysics 81 (5), S281–S297. https://doi.org/10.1190/geo2015-0557.1.
Hao, Q., Alkhalifah, T., 2019. Viscoacoustic anisotropic wave equations. Geophysics 84 (6), C323–C337. https://doi.org/10.1190/geo2018-0865.1.
Huang, J., Mao, Q., Mu, X., et al., 2024. Least-squares reverse time migration based on an efficient pure qP-wave equation. Geophys. Prospect. 72 (4), 1290–1311. https://doi.org/10.1111/1365-2478.13326.
Kjartansson, E., 1979. Constant-Q wave propagation and attenuation. J. Geophys. Res. 84 (B9), 4737–4748. https://doi.org/10.1029/JB084iB09p04737.
Li, Q., Fu, L.Y., Zhou, H., et al., 2019. Effective Q-compensated reverse time migration using new decoupled fractional Laplacian viscoacoustic wave equation. Geophysics 84 (2), S57–S69. https://doi.org/10.1190/geo2017-0748.1.
Liang, K., Cao, D., Sun, S., et al., 2023. Decoupled wave equation and forward modeling of qP wave in VTI media with the new acoustic approximation. Geophysics 88 (1), WA335–WA344. https://doi.org/10.1190/geo2022-0292.1.
Liu, H.P., Anderson, D.L., Kanamori, H., 1976. Velocity dispersion due to anelasticity; implications for seismology and mantle composition. Geophys. J. Int. 47 (1), 41–58.
Mao, Q., Huang, J., Mu, X., et al., 2024a. Accurate simulations of pure-viscoacoustic wave propagation in tilted transversely isotropic media. Petrol. Sci. 21 (2), 866–884. https://doi.org/10.1016/j.petsci.2023.11.005.
Mao, Q., Huang, J., Mu, X., et al., 2024b. Efficient pure qP-wave modeling and reverse time migration in tilted transversely isotropic media calculated by a finite-difference approach. Geophysics 89 (6), 1–64. https://doi.org/10.1190/geo2023-0631.1.
McDonal, F.J., Angona, F.A., Mills, R.L., et al., 1958. Attenuation of shear and compressional waves in Pierre shale. Geophysics 23 (3), 421–439. https://doi.org/10.1190/1.1438489.
Mu, X., Huang, J., Wen, L., et al., 2021. Modeling viscoacoustic wave propagation using a new spatial variable-order fractional Laplacian wave equation. Geophysics 86 (6), T487–T507. https://doi.org/10.1190/geo2020-0610.1.
Mu, X., Huang, J., Li, Z., et al., 2022. Attenuation compensation and anisotropy correction in reverse time migration for attenuating tilted transversely isotropic media. Surv. Geophys 43 (3), 737–773. https://doi.org/10.1007/s10712-022-09717-0.
Mu, X., Huang, J., 2023. A simple and high-efficiency viscoacoustic reverse time migration calculated by finite difference. Geophysics 88 (6), S213–S223. https://doi.org/10.1190/geo2022-0762.1.
Qu, Y., Huang, J., Li, Z., et al., 2017. Attenuation compensation in anisotropic least-squares reverse time migration. Geophysics 82 (6), S411–S423. https://doi.org/10.1190/geo2016-0677.1.
Robertsson, J.O., Blanch, J.O., Symes, W.W., 1994. Viscoelastic finite difference modeling. Geophysics 59 (9), 1444–1456. https://doi.org/10.1190/1.1443701.
Shen, Y., Biondi, B., Clapp, R., 2018a. Q-model building using one-way wave-equation migration Q analysis—Part 1: theory and synthetic test. Geophysics 83 (2), S93–S109. https://doi.org/10.1190/geo2016-0658.1.
Shen, Y., Biondi, B., Clapp, R., 2018b. Q-model building using one-way wave-equation migration Q analysis—Part 2: 3D field-data test. Geophysics 83 (2), S111–S126. https://doi.org/10.1190/geo2017-0032.1.
Suh, S., K, Yoon, J., Cai, Wang, B., 2012. Compensating visco-acoustic effects in anisotropic reverse-time migration. In: 82th Annual International Meeting, SEG, Expanded Abstracts, pp. 316–3164. https://doi.org/10.1190/segam2012-1297.1.
Sun, J., Zhu, T., 2018. Strategies for stable attenuation compensation in reverse-time migration. Geophys. Prospect. 66 (3), 498–511. https://doi.org/10.1111/1365-2478.12579.
Thomsen, L., 1986. Weak elastic anisotropy. Geophysics 51 (10), 1954–1966. https://doi.org/10.1190/1.1442051.
Tsvankin, I., 1996. P–wave signatures and notation for transversely isotropic media: an overview. Geophysics 61 (2), 467–483. https://doi.org/10.1190/1.1443974.
Tian, K., Huang, J., Bu, C., Li, G., Yan, X., Lu, J., 2015. Viscoacoustic reverse time migration by adding a regularization term. In: SEG International Exposition and Annual Meeting. https://doi.org/10.1190/segam2015-5932246.1. SEG-2015.
Usher, P.J., Kendall, J.M., Kelly, C.M., et al., 2017. Measuring changes in fracture properties from temporal variations in anisotropic attenuation of microseismic waveforms. Geophys. Prospect. 65 (1), 347–362. https://doi.org/10.1111/1365-2478.12551.
Wang, Y., Zhou, H., Chen, H., et al., 2018a. Adaptive stabilization for Q-compensated reverse time migration. Geophysics 83 (1), S15–S32. https://doi.org/10.1190/geo2017-0244.1.
Wang, N., Zhou, H., Chen, H., et al., 2018b. A constant fractional-order viscoelastic wave equation and its numerical simulation scheme. Geophysics 83 (1), T39–T48. https://doi.org/10.1190/geo2016-0609.1.
Wang, N., Zhu, T., Zhou, H., et al., 2020. Fractional Laplacians viscoacoustic wavefield modeling with k-space-based time-stepping error compensating scheme. Geophysics 85 (1), T1–T13. https://doi.org/10.1190/geo2019-0151.1.
Xie, Y., Sun, J., Zhang, Y., et al., 2015. Compensating for visco-acoustic effects in TTI reverse time migration. In: SEG International Exposition and Annual Meeting. https://doi.org/10.1190/segam2015-5855445.1.
Xing, G., Zhu, T., 2023. Compensating the attenuation effects in the full waveform inversion with dissipation-dispersion decoupling. Geophysics 88 (5), R645–R654. https://doi.org/10.1190/geo2022-0614.1.
Xu, S., Zhou, H., 2014. Accurate simulations of pure quasi-P-waves in complex anisotropic media. Geophysics 79 (6), T341–T348. https://doi.org/10.1190/geo2014-0242.1.
Xu, S., Stovas, A., Alkhalifah, T., et al., 2020. New acoustic approximation for transversely isotropic media with a vertical symmetry axis. Geophysics 85 (1), C1–C12. https://doi.org/10.1190/geo2019-0100.1.
Xu, W., Li, Z., Wang, J., et al., 2015. A Pure viscoacoustic equation for VTI media applied in anisotropic RTM. J. Geophys. Eng. 12 (6), 969–977. https://doi.org/10.1088/1742-2132/12/6/969.
Yang, J., Zhu, H., 2018. A time-domain complex-valued wave equation for modelling visco-acoustic wave propagation. Geophys. J. Int. 215 (2), 1064–1079. https://doi.org/10.1093/gji/ggy323.
Yang, P., Brossier, R., Métivier, L., et al., 2016. A review on the systematic formulation of 3-D multiparameter full waveform inversion in viscoelastic medium. Geophys. J. Int. 207 (1), 129–149. https://doi.org/10.1093/gji/ggw262.
Ye, Z., Huang, J., Mu, X., et al., 2024. Multidimensional Q-compensated reverse time migration using a high-efficient decoupled viscoacoustic wave equation. Geophys. Prospect. 72 (6), 2109–2122. https://doi.org/10.1111/1365-2478.13501.
Zhan, G., Pestana, R., Stoffa, P., 2012. Decoupled equations for reverse time migration in tilted transversely isotropic media. Geophysics 77 (2), T37–T45. https://doi.org/10.1190/geo2011-0175.1.
Zhang, Y., Liu, Y., Xu, S., 2020. Anisotropic viscoacoustic wave modelling in VTI media using frequency-dependent complex velocity. J. Geophys. Eng. 17 (4), 700–717. https://doi.org/10.1093/jge/gxaa023.
Zhou, H., Zhang, G., Bloor, R., 2006. An anisotropic acoustic wave equation for modeling and migration in 2D TTI media. In: 76th Annual International Meeting, SEG, Expanded Abstracts, pp. 194–198. https://doi.org/10.1190/1.2369913.
Zhu, Y., Tsvankin, I., Vasconcelos, I., 2007. Effective attenuation anisotropy of thin-layered media. Geophysics 72 (5), D93–D106. https://doi.org/10.1190/1.2754185.
Zhu, T., Carcione, J., Harris, J.M., 2013. Approximating constant-Q seismic propagation in the time domain. Geophys. Prospect. 61 (5), 931–940. https://doi.org/10.1111/1365-2478.12044.
Zhu, T., Harris, J.M., 2014. Modeling acoustic wave propagation in heterogeneous attenuating media using decoupled fractional Laplacians. Geophysics 79 (3), T105–T116. https://doi.org/10.1190/geo2013-0245.1.
Zhu, T., 2016. Implementation aspects of attenuation compensation in reverse-time migration. Geophys. Prospect. 64 (3), 657–670. https://doi.org/10.1111/1365-2478.12301.
Zhu, T., Bai, T., 2019. Efficient modeling of wave propagation in a vertical-transversely isotropic attenuative medium based on fractional Laplacian. Geophysics 84 (3), T121–T131. https://doi.org/10.1190/geo2018-0538.1.
Zhubayev, A., Houben, M.E., Smeulders, D.M., et al., 2016. Ultrasonic-velocity and attenuation anisotropy of shales, Whitby, United Kingdom. Geophysics 81 (1), D45–D56. https://doi.org/10.1190/geo2015-0211.1.